

THE PIONIC SODIUM 2p-1s TRANSITION

by

DAVID IORWERTH BRITTON

B.Sc., University of Nottingham, 1979

A THESIS SUBMITTED IN PARTIAL FULFILLMENT
OF THE REQUIREMENTS FOR THE DEGREE OF

MASTER OF SCIENCE

in the Department

of

Physics

ACCEPTED

DIES

DEAN


DATE

1984: 12: 14

We accept this thesis as conforming
to the required standard


G.R. Mason


A. Olin


L.P. Robertson


T.W. Dingle


A. Kirk

© DAVID IORWERTH BRITTON, 1984

UNIVERSITY OF VICTORIA

August 1984

QC 793.5

M427 B7


ABSTRACT

Joint Supervisors: Dr Grenville Mason and Dr Arthur Olin.

A recurring feature in the global analysis of pionic X-ray data has been the anomalous width of the π -Na 2p-1s X-ray. Previous experimental data has shown widths of up to 12KeV, whilst optical model calculations predict values no smaller than 17KeV. In order to resolve this discrepancy another measurement has been made using a newly-developed Compton suppression spectrometer. The performance of the suppression system with sources and in beam, is reported. The resulting reduction of the continuum Compton background by a factor of about 5 at the energy of the X-ray, has allowed a more confident determination of the X-ray width and energy. The values obtained are:

π Na 2p-1s X-ray: Energy = 276.2(0.9)KeV Width = 16.7(3.1)KeV

EXAMINERS:


G.R. Mason
A. Olin
T.W. Dingle
L.P. Robertson
A. Kirk

CONTENTS

ABSTRACT	ii
CONTENTS	iii
LIST OF TABLES	v
LIST OF FIGURES.	vi
ACKNOWLEDGEMENTS	viii
DEDICATION	ix

<u>CHAPTER</u>	<u>PAGE</u>
1. INTRODUCTION	1
2. THEORETICAL OUTLINE	
The Electromagnetic System.	5
The Idea of an Optical Potential.	8
The Optical Model.	11
The Granular Structure of Nuclear Matter	14
Pion Absorption	17
Results of the Optical Model	19
3. THE EXPERIMENTAL METHOD	
Introduction	25
Experimental Arrangement	27
Detection System	30
The Electronics:	32
Telescope logic	33
Germanium Logic	34
BGO Logic	36
Trigger Logic	37
4. THE COMPTON SUPPRESSION SYSTEM	
Introduction	40
Principle of the Suppression System.	44
Construction of the Suppressor	45
Operation of the Suppressor	47
Performance of the Suppression System	51
Conclusion	58

5.	THE ANALYSIS	
	Introduction	59
	The Peak Fitting Program JAGSPOT.	60
	Calibration.	62
	The Detector Response	64
	Analysis of the Sodium X-ray	69
6.	DISCUSSION OF RESULTS AND CONCLUSION	
	Theoretical Shifts and Widths.	78
	Experimental Conclusions	81
	Comparison of Results	83
	Conclusion	85
	REFERENCES	86

LIST OF TABLES

<u>Table</u>	<u>PAGE</u>
1. The Calibration Peaks.	62
2. Tailing Data.	65
3. Results	76
4. Contributions to the Uncertainties	76
5. Optical Model Fits of Sodium	79
6. The Optical Potential Parameters	79
7. Results for the Energies, Widths and Shifts of the Pionic 2p-1s X-ray in Sodium	82

LIST OF FIGURES

<u>Figure</u>	<u>Page</u>
1. Effect of the Strong Interaction	2
2. Fits to Pionic Atom Data.	24
3. Low Energy Pion Channel M13.	26
4. The Experimental Arrangement	29
5. The Telescope Logic	33
6. The Germanium Logic	34
7. The BGO Logic	36
8. The Trigger Logic	37
9. The Complete Electronics.	39
10. Photon Absorption in Germanium.	41
11. Angular Distribution of Compton Scattering.	43
12. Schematic of the Compton Suppression Spectrometer	46
13. BGO Outputs for Two Single Photoelectrons	48
14. BGO Outputs for a Large Signal.	49
15. Suppressed and Unsuppressed ^{60}Co Spectra	52
16. Suppressed and Unsuppressed Prompt Spectra.	54
17. Counts Removed by the Suppression System	55
18. Suppressed and Unsuppressed Delayed Spectra	56
19. Suppressed and Unsuppressed Source Spectra.	57

<u>Figure</u>	<u>Page</u>
20. Fit of the Calibration Data.	63
21. FWHM as a Function of Energy	66
22. Selenium Source Spectrum.	67
23. Relative Efficiency from Selenium Source	68
24. The Fitted regions.	70
25. Peaks in the Normal Fit Region.	71
26. Extrapolated Fit from the Smallest Region	73
27. Contaminants near the Centroid of the X-ray	74
28. The Best Fit.	77

ACKNOWLEDGEMENTS

I would like to acknowledge the work of the mesic X-ray group who performed this experiment, including G. Beer, R. Kunselman, J. Macdonald, G. Marshall, G. Mason, T. Numao, A. Olin, and B.H. Olaniyi. I would like to thank P. Poffenberger for his additional work on the Compton Suppressor and for help with this thesis. My thanks also go to the members of my committee for their help refining this thesis, and to Sue Cannon for lettering the dedication.

My final thanks go to my joint supervisors: Dr. Art Olin for his considerable help and encouragement at all stages of this project, and Dr. Gren Mason all for his assistance over the last two years.

Dedication

To My Parents

CHAPTER 1: INTRODUCTION.

In 1935 Yukawa proposed that the strong interaction was mediated by an exchange particle called the meson (YU35). This was in analogy to the well established idea that charged particles communicated by the exchange of photons. In 1947 the pi-meson, or pion, was seen in cosmic rays (LA47), and identified with the Yukawa meson. Shortly after this, it was produced by an accelerator for the first time (GA48).

Almost immediately, the existence of mesic atoms was predicted by both Wheeler (WH47) and by Fermi and Teller (FE47). A pionic atom is formed when a negatively charged pion is slowed down in matter, and captured by an atom into a high atomic orbit. The pion then cascades down to lower energy orbits, first by Auger electron processes, and then by the emission of X-rays. The cascade process breaks off when the wave function of the pion starts to overlap with the nucleus. The pion then interacts strongly, and is absorbed by the nucleus.

Due to its large mass relative to the electron, the pion spends most of its atomic life within the electron cloud. This means that the pionic atom can be treated like a hydrogen-atom, and the higher energy levels can be calculated from electromagnetic theory. However, once the pion gets close enough to the nucleus to feel the effects of the strong interaction, the energy levels are perturbed. In general this effect is only significant for the lowest level before absorption by the nucleus. This is a reflection of the short range of the strong

interaction, which leads to a change of several orders of magnitude in the effect for each step in orbital quantum number, ℓ . So there arises a last observable X-ray transition that is shifted in energy from that expected with purely electromagnetic considerations.

In addition, the pion's lifetime in an orbit where it feels the strong interaction, is very short. The uncertainty principle thus dictates that the width of the energy level in this orbit satisfies $\Delta E \cdot \Delta t > \hbar$. Thus the lowest energy level is subject to 'absorptive broadening', as well as to the strong interaction shift mentioned above. Experimentally, these effects are evident as a broadened X-ray line, whose centroid is shifted from the position expected from a purely electromagnetic interaction.

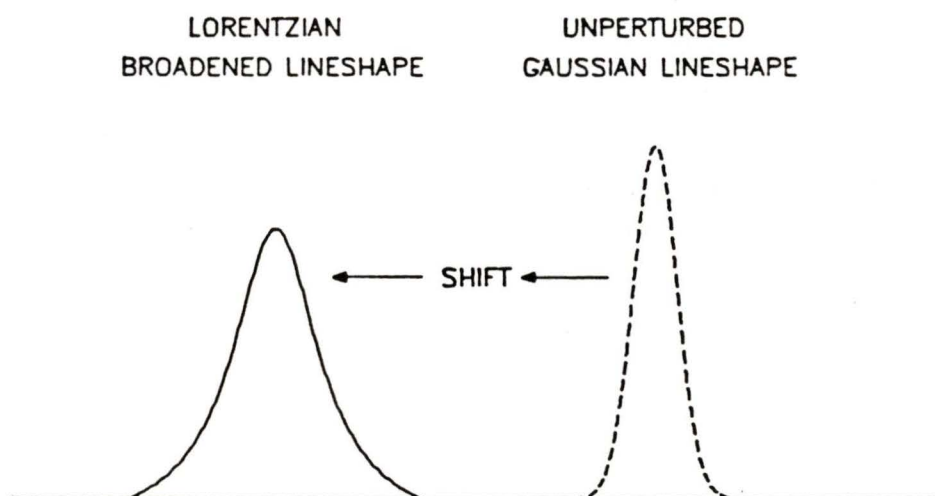


Figure 1. Effect of Strong Interaction.

The theoretical approach to describing pionic atoms started with an attempt to deduce the strong interaction width and shift from low energy π^- -nucleon scattering data using first order perturbation theory. However, the pion wavefunction is modified by the strong interaction which wasn't accounted for in the perturbation treatment, and so this led to a phenomenological approach using a pion-nuclear potential derived by Ericson and Ericson (ER66). Over the last decade, much work has achieved generally good agreement between experimental and theoretical widths and shifts. Unfortunately, certain elements, including sodium, have remained in disagreement.

The primary aim of this thesis project was to obtain a new measurement of the strong interaction width and shift of the pionic sodium 2p-1s X-ray. The data analysed was obtained by the University of Victoria Mesic X-ray group in June 1983, as part of a series of experiments to investigate the 2p-1s transition in light nuclei. The experiment made use of a newly-developed Compton suppression system that reduced an important background due to Compton scattered photons, thus allowing a much better measurement to be made. The second aim of this thesis is, therefore, to describe the construction of the Compton suppressor, and its performance as determined from tests prior to, and during, the X-ray experiment.

My contribution to this project started with the testing of the newly-constructed suppressor with sources. Then I helped set up

the X-ray experiment and the data acquisition electronics. I assisted with the running of the experiment and with the on-line analysis. Finally, I was principally responsible for the analysis of the sodium data.

For the sake of completeness, the main steps in the theoretical description of pionic atoms are outlined in Chapter 2, which illustrates in more detail the motivation behind this measurement. In Chapter 3 the details of the experiment are discussed, and Chapter 4 contains a description of the Compton suppression system. Chapter 5 is devoted to the analysis of the data obtained in this experiment. Finally, in Chapter 6, the results are discussed and compared both with theoretical predictions and with previous experimental results.

CHAPTER 2: THEORETICAL OUTLINE

The Electromagnetic System.

The atomic levels observed when a negative pion is captured by a nucleus arise in the same manner as the electronic levels in a hydrogen atom. This is true because the relatively large mass of the pion means that it spends most of its time in orbits closer to the nucleus than the electron cloud, which can therefore be ignored. In consequence the simple Bohr formulas lead to a good description of the energy levels:

$$E_n = - \frac{\mu c^2}{2} \left(\frac{Z\alpha}{n} \right)^2 \quad (1)$$

$$r_n = \frac{\hbar^2}{\mu e^2} \frac{n^2}{Z}$$

where E_n is the energy of an atomic level of principle quantum number 'n', and r_n is the radius of the corresponding Bohr orbit. ' α ' = 1/137 is the fine structure constant, and μ is the reduced mass of the moving particle.

The actual behaviour of such an atomic system is described more completely by the relativistic Klein-Gordon equation, since the pions are bosons with spin=0. The energy eigenvalues for a point nucleus are:

$$E_{n,\ell} = -\frac{\mu c^2}{2} \left(\frac{\alpha Z}{n}\right)^2 \left[1 + \left(\frac{\alpha Z}{n}\right)^2 \left(\frac{n}{\ell+1/2} - \frac{3}{4}\right) - \dots\right] \quad (2)$$

where n and ℓ are the principle and orbital quantum numbers respectively. This expression is valid for $2Z\alpha < 1$ (otherwise it would diverge) and ignores terms of order $(\alpha Z)^6$, and higher.

In practice the nuclear charge has a finite extension so the above energy levels, E_{KG} must be modified by a correction E_{FE} . This 'finite extension' correction accounts for the overlapping of the meson wavefunction and the charge distribution of the nucleus which results in a smaller effective charge. Therefore the binding energy is reduced.

Another effect that must be accommodated is that of vacuum polarization which describes the production of virtual e^+, e^- pairs in the coulomb field and results in an increase of the potential produced by the nuclear charge. Denoting this term by E_{vp} , which increases the binding energy, the purely electromagnetic energy levels may be described as:

$$E_{em} = E_{KG} + E_{FE} + E_{vp} \quad (3)$$

In addition to these electromagnetic effects, the pion is subject to the strong interaction with the nucleus. Because of the short range nature of this interaction, the effect is only important when the pion is close to the nucleus. The lowest energy levels must

now be described as:

$$E = E_{KG} + E_{FE} + E_{vp} + E_N \quad (4)$$

where E_N is the shift due to a strong-interaction potential V_N . The Klein-Gordon equation describing the pion-nucleus system is then:

$$\left[\hbar^2 \nabla^2 + \frac{1}{c^2} (E - V_{FS})^2 - \mu^2 c^2 \right] \psi = 2\mu V_N \psi . \quad (5)$$

Here V_{FS} is the coulomb potential corrected for 'finite extension' effects.

The strong interaction shift was first estimated by assuming a square well potential up to the nuclear radius, and then applying perturbation theory, to obtain the energy shifts.

However, the problem with this approach is that the strong interaction changes the pion wavefunction which, in turn, modifies the finite size and vacuum polarisation effects. In addition it is a great over-simplification to describe the nuclear potential as a square well and whilst the shifts obtained from such, by perturbation expansions, agreed with early data, such a model certainly did not account for the absorptive broadening of the lineshape.

The Idea of an Optical Potential.

The most common approach to describe the effects of the strong interaction, is a phenomenological theory based on the elementary processes

$\pi^- + N \longrightarrow \pi^- + N$ elastic scattering, and

$\pi^- + N + N \longrightarrow N + N$ pion absorption.

which describes the πN interaction in terms of an optical potential,

$$V_{\text{opt}} = \text{Re}(V) + i\text{Im}(V) \quad (6)$$

This arises in analogy to the conventional optical theory that describes the modification of a plane wave incident on a many-particle system. In this theory, the original plane wave, of propagation vector k , is modified by each layer of scatterers to a wave described by k' . The ratio of k/k' is known as the refractive index, and both this and the propagation vector, contain imaginary terms. This imaginary part, whose presence represents the loss in the forward propagated wave, is related to the total cross section through the optical theorem.

$$\text{Im}(f) = \frac{k \sigma_{\text{total}}}{4\pi} \quad (7)$$

where f is the forward scattering amplitude.

In the case of an incident pion, rather than a plane wave, the motion is attributed to a potential V and the loss in the forward beam is again represented by an imaginary term, which now appears in the potential V . However, in this case, 'real' absorption of the pion can occur on a nucleon and, by analogy, this is also incorporated as an imaginary term in the potential.

In a mesic atom, the bound pion is regarded as a wave scattered off the nucleus, and ignoring nuclear absorption, its interaction with the nucleus is a kind of low energy elastic scattering [ER70]. This relationship can be seen by introducing a short range pseudopotential, $V(\underline{r})$, for which the scattering amplitude $f(\theta)$ is:

$$f(\theta) = -\frac{2m}{4\pi} \int e^{-i\underline{k}\cdot\underline{r}} V(\underline{r}) e^{i\underline{k}'\cdot\underline{r}} d\underline{r} . \quad (8)$$

Treating the potential as a perturbation, the energy shift is given by:

$$\Delta E_{n\lambda} = \int V(\underline{r}) |\psi_{n\lambda}|^2 d\underline{r} . \quad (9)$$

Substitution of the pion bound state wavefunction into Equation 9 gives the result [ER70]:

$$\Delta E_{n\lambda} \propto \int r^{2\lambda} V(\underline{r}) d^3r . \quad (10)$$

The scattering amplitude (Equation 8) can be expanded as a series of partial waves, and if the leading term of the λ 'th partial

wave is projected out, its corresponding potential scattering length, A_ℓ , can be shown to be (ER70):

$$A_\ell = - \frac{2m\pi}{4\pi} \int \frac{r^{2\ell}}{([2\ell+1]!!)^2} V(\underline{r}) d^3r \quad (11)$$

As can be seen from the last two equations, both the energy shift and the scattering length, due to the ℓ 'th partial wave, have a common dynamical factor:

$$\int r^{2\ell} V(\underline{r}) d\underline{r} \quad . \quad (12)$$

This shows that the energy shift of the bound state n, ℓ is directly related to the elastic scattering partial wave amplitude.

The Optical Model.

Since the theory that is to be used is partly based upon elementary πN elastic scattering, it is convenient to start with an expression for this free scattering amplitude. This is immediately extended to describe the scattering of the pion off the i 'th nucleon in the nucleus by evoking the impulse approximation. This assumes that the scattering amplitude of pions from free and bound nucleons is the same, apart from kinematical factors. The approximation is expected to be good for the low pion energies that are relevant here (ER66). So following Ericson and Ericson, the πN scattering amplitude ' $f_i(\theta)$ ' for the i 'th nucleon is given as:

$$f_i(\theta) = b_0 + b_1 \underline{t} \cdot \underline{\tau} + [c_0 + c_1 \underline{t} \cdot \underline{\tau}] \underline{k} \cdot \underline{k}' - i[d_0 + d_1 \underline{t} \cdot \underline{\tau}] \underline{\sigma} \cdot \underline{k} \times \underline{k}' \quad (13)$$

Here \underline{k}' and \underline{k} are the momenta of the scattered and incident pion; \underline{t} is its isospin; $\underline{\tau}$ and $\underline{\sigma}$ are the isospin and spin of the nucleon.

The constants in Equation 13 can be expressed in terms of conventional s-wave scattering lengths, and p-wave scattering volumes; α_{2t} and $\alpha_{2t,2j}$ respectively, where t is the isospin of the πN system and j is its spin.

$$b_0 = 1/3(\alpha_1 + 2\alpha_3)$$

$$b_1 = 1/3(\alpha_3 - \alpha_1)$$

$$\begin{aligned}
c_0 &= 1/3(4\alpha_{33} + 2\alpha_{13} + 2\alpha_{31} + \alpha_{11}) \\
c_1 &= 1/3(2\alpha_{33} - 2\alpha_{13} + \alpha_{31} - \alpha_{11}) \\
d_0 &= 1/3(2\alpha_{31} - 2\alpha_{33} + \alpha_{11} - \alpha_{13}) \\
d_1 &= 1/3(\alpha_{31} - \alpha_{33} - \alpha_{11} + \alpha_{13}).
\end{aligned}
\tag{14}$$

Equation 13 represents the s-wave interaction (first two terms), and the p-wave interaction. It has been shown by Partenshi and Ericson (PA67) that the contribution from higher ℓ -states can be neglected. In addition, the terms associated with d_0 and d_1 are spin dependent terms whose magnitude has been estimated, most recently, by Friedman (FR80) and they can be ignored.

To obtain the total scattering amplitude the above component must be summed over all the nucleons in the nucleus. This is done under the frozen nucleus approximation where the positions of the nucleons are assumed to be undisturbed by the scattering pion; that is, nuclear recoil effects are ignored.

This first approximation to the total scattering amplitude is attributed to a pseudo-potential which is found by the inversion of the plane wave Born approximation that relates the scattering amplitude to a potential:

$$V(\underline{r}) = - \frac{2\pi\hbar^2}{m} \int f(\theta) e^{-i(\underline{k}-\underline{k}')\cdot\underline{r}} d^3(\underline{k}-\underline{k}') \tag{15}$$

Then the identity;

$$\underline{k} = -i(\underline{\nabla} e^{i\mathbf{k}\cdot\mathbf{r}})e^{-i\mathbf{k}\cdot\mathbf{r}} \quad (16)$$

is used, which transforms the $\underline{k}\cdot\underline{k}'\rho(\mathbf{r})$ terms to the form $\underline{\nabla}\rho(\mathbf{r})\underline{\nabla}$. Which then yields a nuclear potential:

$$\begin{aligned} V_N(\underline{\mathbf{r}}) = & -\frac{2\pi\hbar^2}{\mu_\pi} \{b_0\rho(\underline{\mathbf{r}}) + b_1[\rho_n(\underline{\mathbf{r}}) - \rho_p(\underline{\mathbf{r}})] \\ & + \underline{\nabla} \frac{1}{F} (c_0\rho(\underline{\mathbf{r}}) + c_1[\rho_n(\underline{\mathbf{r}}) - \rho_p(\underline{\mathbf{r}})])\underline{\nabla}\} \quad (17) \end{aligned}$$

where $\rho(\underline{\mathbf{r}}) = \rho_n(\underline{\mathbf{r}}) + \rho_p(\underline{\mathbf{r}})$ is the sum of the neutron density, ρ_n , and proton density, ρ_p . μ_π is the reduced mass of the pion-nucleus system. (The kinematical factors which transform the coordinates from the pion-nucleon to the pion-nucleus centre of mass frame, have been omitted.)

This is the velocity dependent potential originally derived by Kisslinger from Watson multiple scattering theory. (KI55, WA53).

The Granular Structure of Nuclear Matter.

It became apparent when theoretical and experimental level shifts were compared, that the first approximation derived so far, was not sufficient. In particular the assumption of a homogeneous nucleus, that has been implicit so far, must be replaced with a description including nucleon-nucleon correlations.

This granular property of nuclear matter gives rise to two effects. It causes the s-wave to be repulsive, and it leads to the Lorentz-Lorenz effect in the p-wave interaction.

The effect on the s-wave is shown by replacing the normal field seen by the incident wave, with an effective field due to the correlation of pairs of nucleons. This describes how the nucleons are distributed close to a certain position. In particular, if that position is the location of a scatterer then the pion views the nucleon as concentrated to a point, surrounded by a hole in the nuclear medium. The effective field within the hole is given by the overall average field, modified by the removal of uniform matter within the hole (ER70).

$$\phi^{\text{eff}} = \frac{1}{1 + a \left\langle \frac{1}{r} \right\rangle_{\text{hole}}} \phi^{\text{ave}} \quad (18)$$

Since this may just be interpreted as a modification of the potential, the scattering length 'a' can be replaced by an effective

scattering length:

$$a \rightarrow a_{\text{eff}} = \frac{a}{(1 + a \langle \frac{1}{r} \rangle_{\text{hole}})} \approx a - a^2 \langle \frac{1}{r} \rangle_{\text{hole}} \dots \quad (19)$$

The linear term in 'a' is small, and the domination of the squared term leads to the repulsive nature of the modified s-wave interaction. The main contribution to this effect is recognisable in a momentum representation as simply the Pauli exclusion principle, which excludes those transitions where a pion scatters a nucleon into a state already occupied by another nucleon. This is known as Pauli blocking. In coordinate space, this restriction gives rise to the longest range correlations : $\langle 1/r \rangle_{\text{corr}} = \langle 1/r \rangle_{\text{hole}}$.

The correlations also give rise to the important Lorentz-Lorenz effect in the p-wave interaction. This arises in analogy to the optical phenomenon that occurs when long wavelength photons traverse matter. In this case the dipole interaction prevails and the short range atom-atom correlations result in a non-linear dependence of the scattering on the medium density. The dipole component of π -nucleon scattering, which arises from the p-wave interaction, results in a similar nonlinear dependence on the nuclear density, when the nucleon-nucleon correlations are considered.

The Lorentz-Lorenz effect can be exhibited by a factor f ,
(ER66)

$$f = 1 + \xi \frac{4\pi}{3} \{c_0 \rho(\underline{r}) + c_1 [\rho_n(\underline{r}) - \rho_p(\underline{r})]\} \quad (20)$$

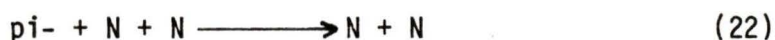
which is used to modify the gradient term of the nuclear potential (Equation 17):

$$\frac{\nabla}{1 + \xi \frac{4\pi}{3} \{c_0 \rho(\underline{r}) + c_1 [\rho_n(\underline{r}) - \rho_p(\underline{r})]\}} \frac{\nabla}{\{c_0 \rho(\underline{r}) + c_1 [\rho_n(\underline{r}) - \rho_p(\underline{r})]\}} \quad (21)$$

It can be seen that $\xi = 0$ reproduces Equation 17, which means no correlation, and $\xi = 1$ corresponds to the short range correlations from Pauli blocking. Some calculations have indicated very short range correlations between nucleons, with $\xi > 1$. (P080)

Pion Absorption.

If the nuclear potential outlined so far, V_N , is to describe the complete interaction, pion absorption must be included. This absorption process is characterised by the fact that in nuclear matter it must occur on a pair of nucleons.



This constraint arises from the conservation of energy and momentum, which dictate that a single nucleon would require too great a Fermi momentum for absorption to take place. This has led to the description of pion absorption in terms of a quasi-deuteron model, where the absorption is assumed to be similar to that on free deuteron, except for scale factors.

Just as the 'optical absorption' was incorporated as an imaginary term, this 'real absorption' is included in the model by adding an imaginary part to both the local and gradient terms of the potential. Thus the nuclear potential of Equation 17 is modified (BA70, for example) to the form:

$$V_N(\underline{r}) = - 2\pi \frac{\hbar^2}{2\mu} \{ b_0 \rho(\underline{r}) + b_1 [\rho_n(\underline{r}) - \rho_p(\underline{r})] + i \operatorname{Im} B_0 \rho^2(\underline{r}) \\ + \underline{\nabla} \frac{1}{f} (c_0 \rho(\underline{r}) + c_1 [\rho_n(\underline{r}) - \rho_p(\underline{r})] + i \operatorname{Im} C_0 \rho_2(\underline{r})) \underline{\nabla} \} \quad (23)$$

where the factor f , describing the Lorentz-Lorenz effect from the short range nucleon correlations, is now expressed as:

$$f = \left\{ 1 + \frac{4\pi}{3} (c_0 \rho(\underline{r}) + c_1 [\rho_n(\underline{r}) - \rho_p(\underline{r})] + i \operatorname{Im} C_0 \rho^2(\underline{r})) \right\} \quad (24)$$

For simplicity, Equation 23 above can be written in the form:

$$2\mu V_N(\underline{r}) = q(\underline{r}) + \underline{\nabla} \cdot \alpha(\underline{r}) \underline{\nabla} \quad (25)$$

where $q(\underline{r})$ and $\alpha(\underline{r})$ are obvious from inspection.

Equation 23 above, represents the complete nuclear potential used to describe the strong interaction effects of the πN system. This complex potential, V_N , is then introduced into the Klein-Gordon equation (Equation 5) and the solution to this yields the pionic energy levels (KR69).

Results of the Optical Model.

The optical potential (Equation 23) fails to describe the real levels in pionic atoms if the parameters are taken to be exactly the ones obtained from the elementary interactions πN and πNN . Instead, empirical values are found by considering these as free parameters in a fit to the experimental data. This arises from the fact that there are corrections to the optical potential that have not been included explicitly, such as the effect of nucleon binding, and other unknown nuclear medium effects. Comparison of these empirical parameters with those obtained from the elementary processes, shows that only b_0 differs significantly, and this can be accounted for when the Pauli correlations are included [TA74].

This procedure, wherein the optical model parameters are optimised through fits to some set of experimental data, is referred to as a 'global fit'. Such fits have been made by several groups, including Tauscher and Schneider (TA74), who looked at the parameter b_0 ; Powers et al. (PO80); Poffenberger (POF80); and Batty, Friedman and Gal in 1983 (BA83).

The result of this phenomenological approach to the πN interaction has been good agreement between experimental and theoretical results, except for the broadest observable transitions to each particular level. In particular, the last observable transition to the 1s level is the pionic ^{23}Na (2p-1s) X-ray. This

has been measured by several groups who found its width to be considerably narrower than predicted. (OL78, BA67, JE66, MI68.)

Batty Friedman and Gal (BA83) performed a particularly interesting analysis where they examined whether the anomalies such as for sodium, set in gradually or abruptly, and attempted to remove these so called 'saturation phenomena' by using several modifications to the optical potential. The first two potentials they tried represented the standard optical potential of Equation 23 with and without the renormalisation due to the Lorentz-Lorenz effect. These are referred to as potentials 1 and 2, respectively.

Another approach that they tried was to use a Laplacian representation of the optical potential, which arises for the following reason:

One of the problems with the Kisslinger potential can be seen by employing the transformation (BA83)

$$v_{\lambda}(\underline{r}) = (1-\alpha(\underline{r}))^{1/2}u_{\lambda}(\underline{r}) \quad (26)$$

which transforms the radial wave function for $u_{\lambda}(\underline{r})$ in the Kisslinger potential to a wave equation for $v_{\lambda}(\underline{r})$ in a potential $U(\underline{r})$ given by:

$$2\mu U(\underline{r}) = -\frac{1}{4} \left(\frac{\alpha'(\underline{r})}{1-\alpha(\underline{r})} \right)^2 - (k^2\alpha(\underline{r}) + \frac{1}{r} \alpha'(\underline{r}) + \frac{1}{2} \alpha''(\underline{r}) - q(\underline{r})) / (1-\alpha(\underline{r})) \quad (27)$$

From this it is apparent that there are un-physical singularities set by the denominator at $\alpha(\underline{r})=1$. A procedure for

smoothing this was suggested by Faldt (FA72), which amounts to replacing the momentum dependent part of the Kisslinger potential $2\mu V^K = \underline{\nabla}\alpha_0(\underline{r}) \cdot \underline{\nabla}$ by the Laplacian potential: $2\mu V^L = -\frac{1}{2}[\Delta\alpha_0(\underline{r})]$. This, by contrast, is momentum-independent, but coincides to first order in nuclear density with the p-wave part of Equation 27.

So in addition to potentials 1 and 2 above, Batty et al. also investigated the behaviour of this Laplacian potential (potential L) and another one, (L*), which they call the renormalised Laplacian potential, with $\xi = 1$.

It has been suggested by Ericson and Tauscher (ER81) that the momentum independent part of the potential should be renormalised with a gauge term. One further potential that Batty et al. tried, investigated this. (Potential C1)

Having established various potentials, including those mentioned above, Batty et al. divided the experimental data into 3 sets. The first set contained the anomalous results: sodium for the 1s level and arsenic and tantalum for the 2p and 3d levels respectively. The second data set was a standard set of high precision measurements from the middle of 1s and 2p data sets, and the third set was an extended set that included the standard set along with elements close to the anomalous results. For example, it included neon, being close to sodium.

They fitted the standard set to establish values for the optical model parameters, and then investigated the effect of fitting

the extended set. The parameters obtained were next used to fit the anomalous results, in order to compare experiment with theoretical predictions. Finally, they attempted a best fit of all the data.

The result of this analysis was that they found all the potentials (except the two Laplacian versions) were equally successful in producing reasonably good fits of the standard, and extended, data sets. The two Laplacian potentials produced a poor fit of the standard data set, which rapidly got worse as the fit was extended.

When the anomalous data set was fitted with the parameters fixed from the extended set, the resulting fit was terrible. A best fit of all the data simply lost the good fit of the extended set without significantly improving the fit to the anomalous cases. These results are summarised in Figure 2.

The conclusions of this analysis, which illustrate the impetus behind the present work, are as follows:

The conventional potentials (that is, not the Laplacian) are all rather equivalent both in their success in fitting the extended set, and in their failure to explain the anomalous results. The failure of the Laplacian potentials provides empirical support for the need of a term $\underline{\nabla} \cdot \alpha(\underline{r}) \underline{\nabla}$, rather than $\nabla^2 \alpha(\underline{r})$ in the optical potential.

In addition, the transition from normal to anomalous is abrupt. In the case of the 1s level this is illustrated by a good fit to

neon, but a poor fit to sodium. Thus the anomaly is either due to a new and unknown effect that sets in suddenly, or to the fact that the experimental width is being masked by some phenomenon.

FITS TO PIONIC ATOM DATA

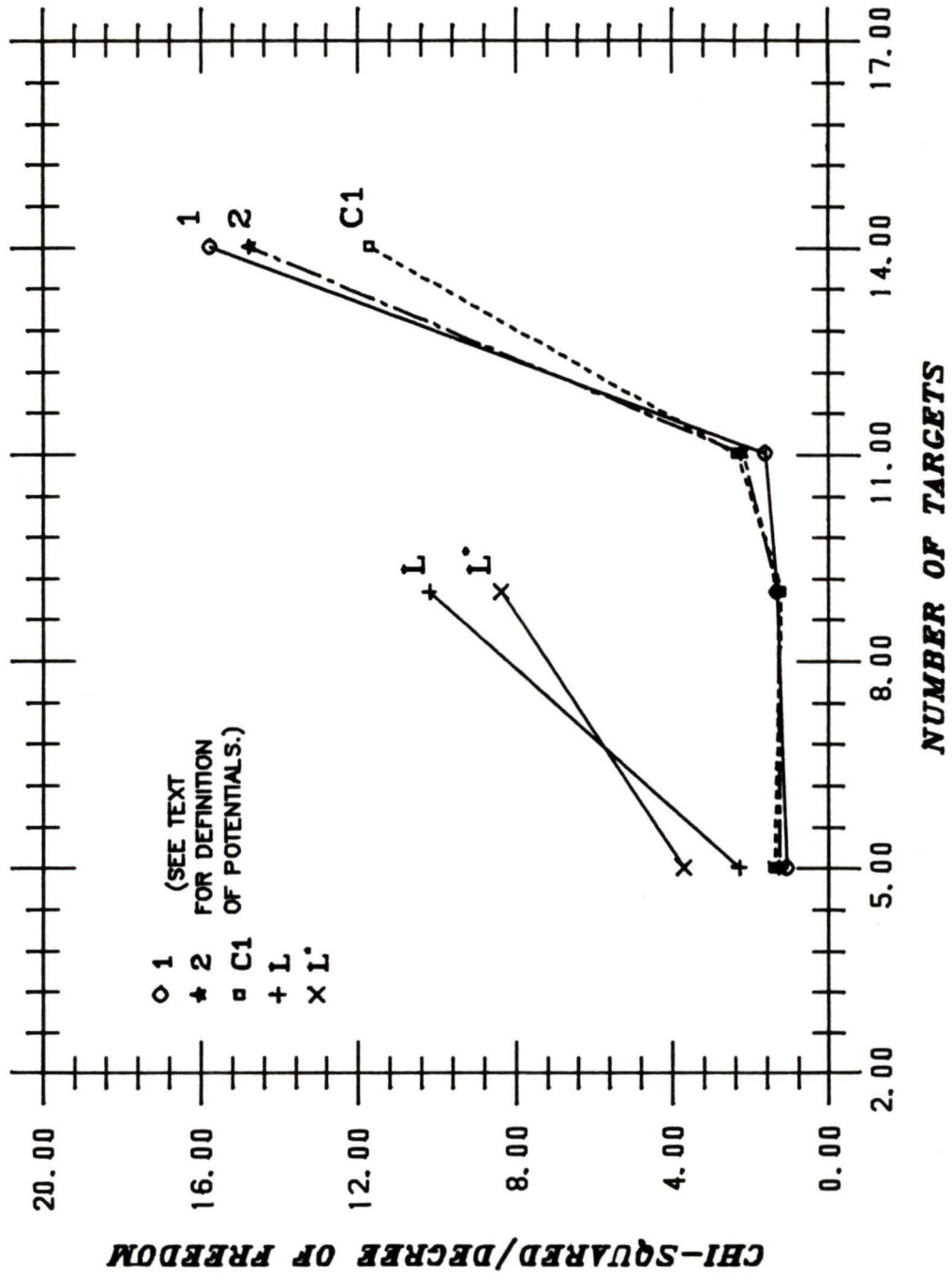


FIGURE 2.

CHAPTER 3: THE EXPERIMENTAL METHOD.

Introduction.

The experiment was performed at the TRIUMF facility situated adjacent to the University of British Columbia in Vancouver B.C. H^- ions are injected into the center of the cyclotron and accelerated up to 500Mev. They are then stripped of their electrons and the resulting proton beam, of up to $130\mu A$, is extracted and directed upon the pion production target T1. A secondary channel called M13 (Figure 3), designed to accommodate a low energy pion beam, takes-off from the production target at an angle of 135 degrees to the forward beam, and provided the flux for this experiment.

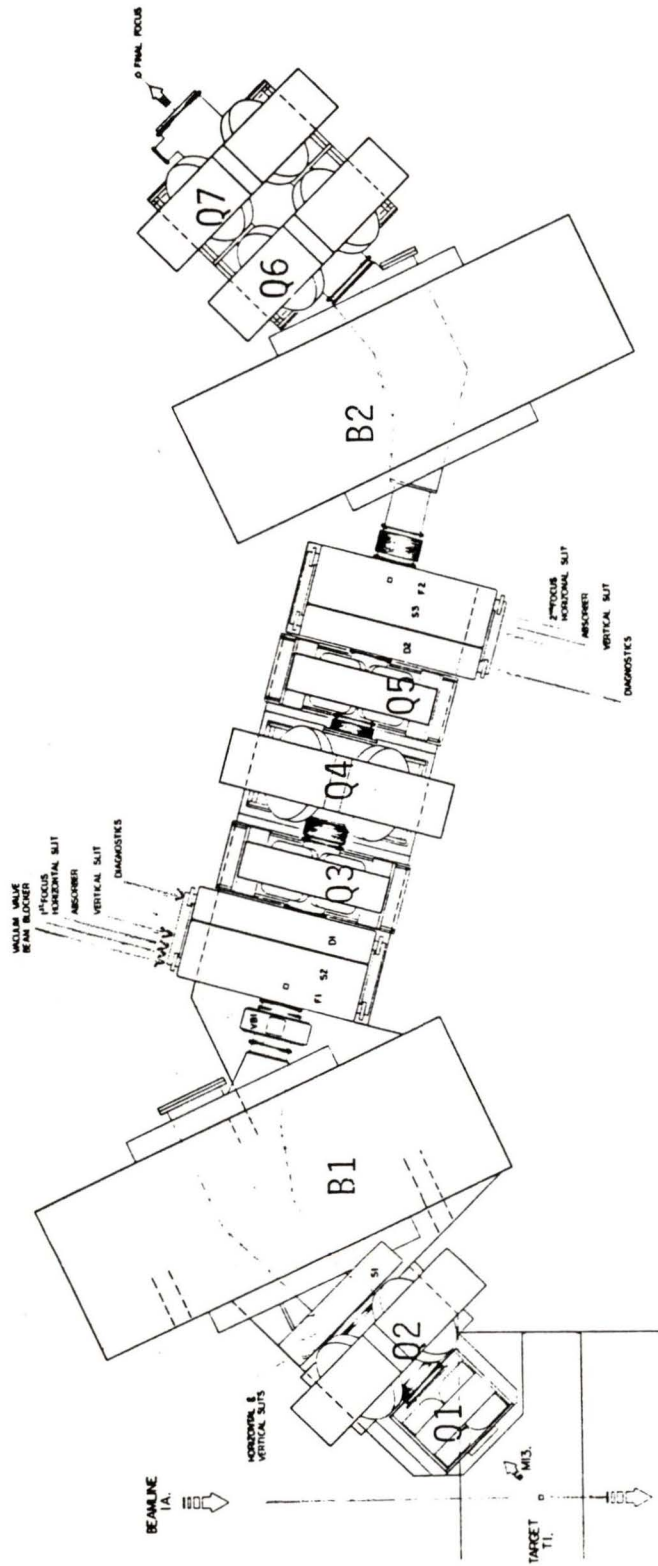


FIGURE 3: Low Energy Pion Channel M13.

Experimental Arrangement

The experiment was set up at the final focus of M13, located 60 cm from the exit of the last quadrupole. A stop in the target was determined by a standard four scintillator telescope which is shown schematically, along with the rest of the experimental arrangement, in Figure 4. Counters S1 and S2 were 10 cm × 10 cm × 0.6 cm and 7.6 cm × 10 cm × 0.16 cm respectively. Counter S3, situated immediately upstream of the target, was chosen to be thin, 0.16 cm, to minimise false stop signals, and was about the same size as the target. The veto counter, S4, was large, 20 cm × 20 cm and was kept downstream to avoid false vetos on particles emitted after a pion stop in the target.

A 1.86 g/cm² beryllium degrader was placed between S2 and S3 to adjust the range of the pions to maximise stops in the target. Beryllium was used since it does not introduce any muonic or pionic X-ray lines into the energy region studied. The exact range of the pions was optimised at the start of the experiment by plotting range curves. These were obtained by scaling the channel momentum up and down and recording the relative number of stops. The channel momentum is scaled by adjusting the currents in the bending magnets B1 and B2, and in the quadrupoles Q1 through Q7 shown in Figure 3 by the same percentage. This changes the momentum that a pion must possess in order to be transported through the channel. The relative number of stops was determined by recording the ratio of 1.2.3.4̄ to 1.2.3 type signals (see Figure 5).

The target consisted of sodium hydride, which was used because of its lower density compared with sodium metal. The lower density means that there is less total material for the same areal density, and a correspondingly smaller probability for the secondary (n,n') reaction, which produces a 440 keV line from sodium, to occur. (The 440 keV gamma has a Compton edge that lies under the X-ray to be measured, and this caused considerable difficulties in previous analyses.) The target container was 6.35 cm in diameter and 1 cm thick. It was constructed out of thin polystyrene to minimise false stops in the holder. Its flat surfaces were 0.005" thick. It was mounted on the downstream side of S3 and at an angle of 45 degrees to the beam to avoid excessive attenuation of the X-rays.

The front of the detector was placed about 36 cm from the beam axis and was shielded with about 4 cm of Densimet collimator, (a tungsten alloy). The beamline side of the detector was shielded with lead bricks. One of the prime concerns when using a germanium detector is that of neutron damage caused by fast neutrons colliding with germanium nuclei. The neutrons are not deflected by the electrostatic force and in consequence can impart sufficient energy in a single collision to knock nuclei from their lattice sites. These nuclei, in turn, produce ionisation while they are charged, but as they slow down they become neutral and can knock further nuclei from the lattice. Thus fast neutrons can rapidly cause radiation damage and these dislocations subsequently become traps for the drifting charge carriers. In order to reduce this the detector was also shielded with borated gypsum bricks which moderate neutrons.

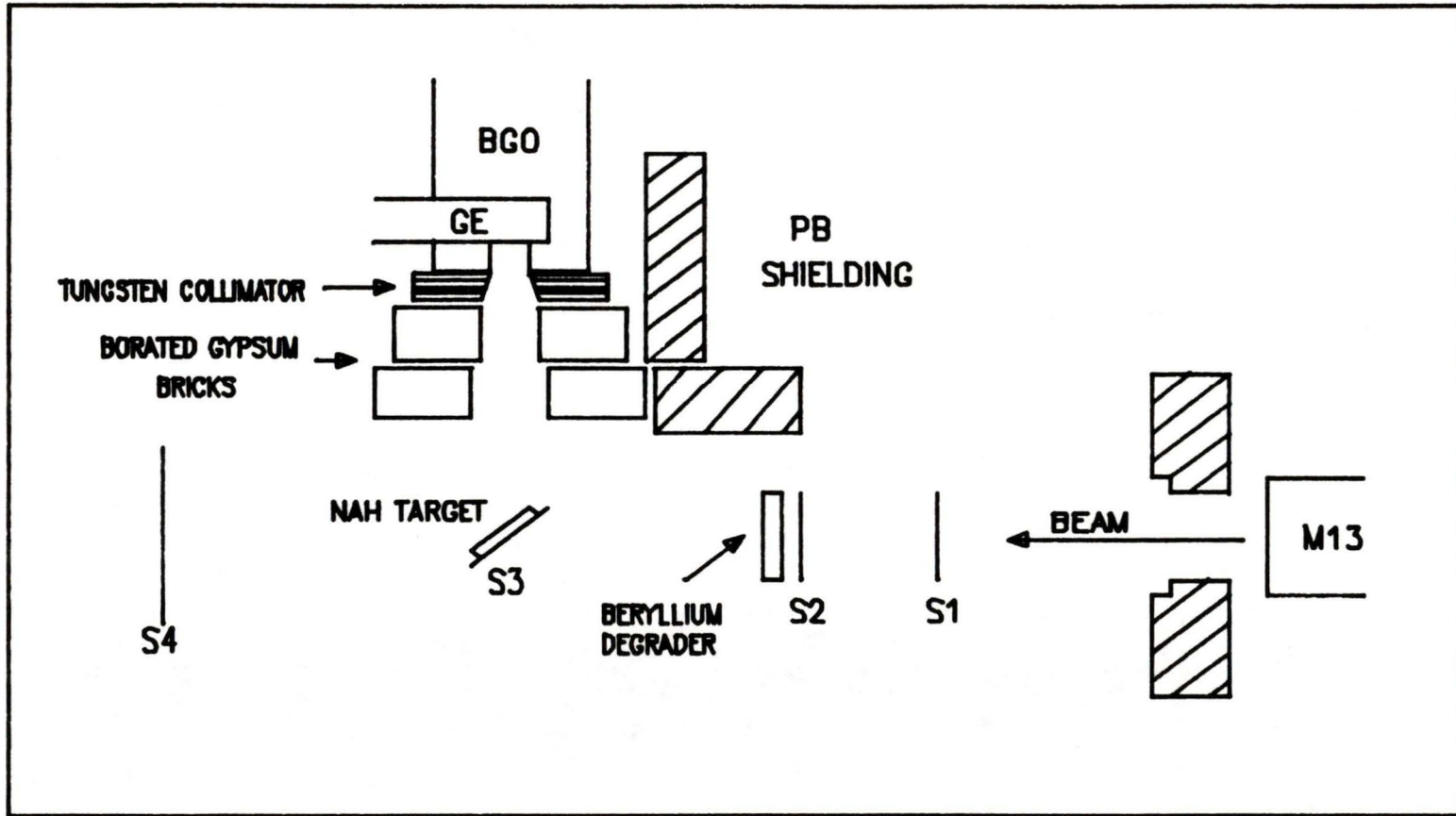


FIGURE 4: The Experimental Arrangement.

Detection System.

The detector consists of a P-type coaxial intrinsic germanium counter, surrounded by a bismuth germanate Compton suppression system.

The Compton suppression system is described more fully in Chapter 4. Briefly, a photon that is Compton scattered from the Ge detector into one of the bismuth germanate crystals, causes a scintillation which is detected in a photomultiplier tube. This in turn is used as a veto signal for the original event in the Ge, thus significantly reducing the prominent Compton background. The bismuth germanate crystals are in fact $\text{Bi}_4\text{Ge}_3\text{O}_{12}$ but it has become conventional to refer, not only to the crystals, but to the whole suppressor, as the BGO.

A good description of the practical design of a high purity germanium detector is given by Goulding and Pehl (G074). A photon incident on the germanium crystal, interacting by the photoelectric effect, may produce a multiplicity of electron-hole pairs proportional to its incident energy. These electrons or holes are collected at the electrodes when a bias voltage is applied across the crystal and the total charge of this output signal is proportional to the full energy of the incident photon. Alternatively, the photon may be Compton scattered out of the germanium crystal and the output signal subsequently collected will not be proportional to the incident energy. This is the origin of the Compton background that the suppression system is designed to reduce.

The resolution of the germanium detector was found to be 1.0(0.1) keV at 276 keV, the energy of the sodium X-ray (see Chapter 5). There are two main contributions to the resolution of a germanium detector in this energy region: the statistical nature of the electron-hole pair production, and the electronic noise in the external amplifying circuit. The two effects add in quadrature to give the full-width-half-max (FWHM) of the resulting spectral line (G074), which is determined experimentally.

Some of the charge produced in the crystal may be trapped at impurities or by defects in the crystal lattice. This produces an excess of pulses in the spectrum on the low energy side of the peak referred to as the low energy tail. This was also determined experimentally (see Chapter 5).

The Electronics.

The data acquisition computer used was a PDP-11/34 and was connected with the experiment via a CAMAC interface. The electronics was divided into four recognisable areas: the telescope logic, the germanium logic, the BGO suppressor logic, and the trigger logic. Each time the trigger logic received an event detected in the germanium counter, the suppressor and the scintillator telescope were examined. If the event was not vetoed by the BGO, and if the event satisfied the stop definition in the telescope logic, a trigger was formed. When this occurred, the trigger logic was disabled whilst the characteristics of the event were recorded on data tape. Once this was completed, the system was reset ready for another event.

Telescope Logic.

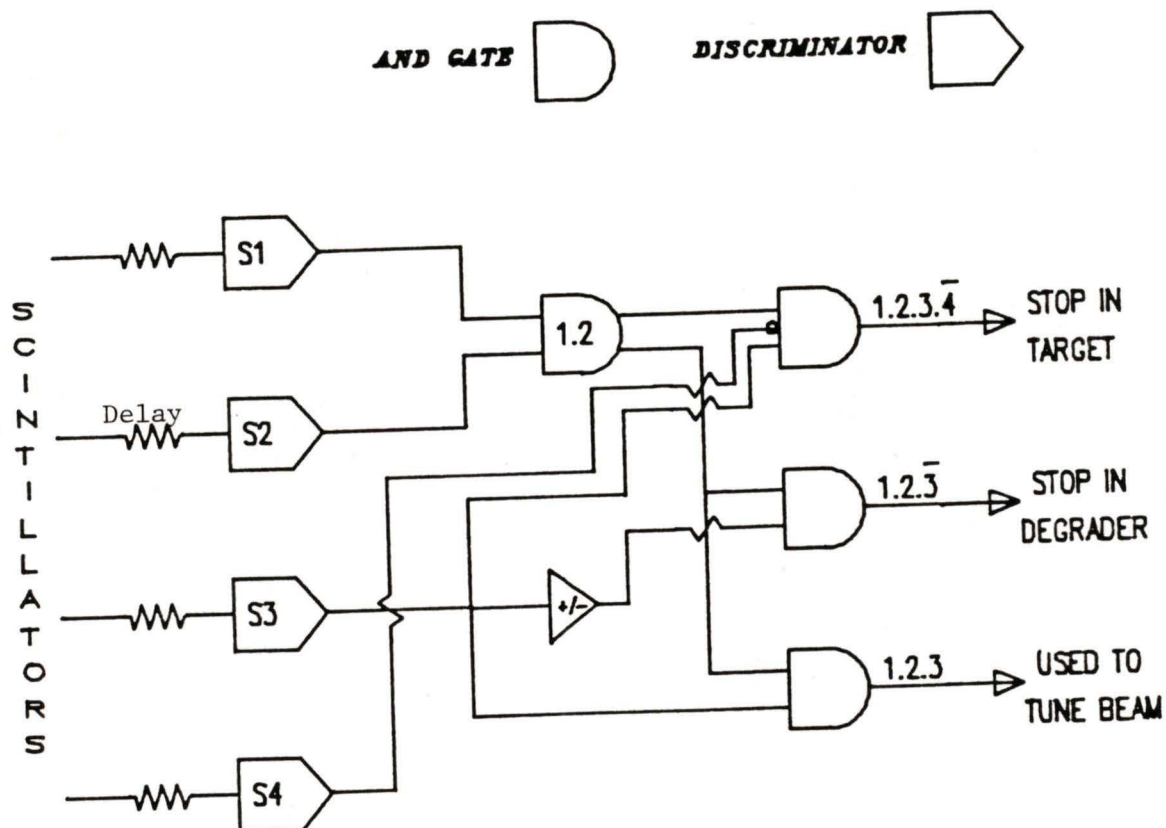


Figure 5: The telescope logic.

The telescope logic required a standard $1.2.3.\bar{4}$ coincidence to define a stop in the target. In addition, a $1.2.\bar{3}$ signal, corresponding to a stop in the degrader, was used to define a gamma source event. The degrader was well shielded from the detector so this latter signal was simply a means of acquiring, under beam conditions, a spectrum from radioactive sources placed adjacent to the detector.

The Germanium Logic.

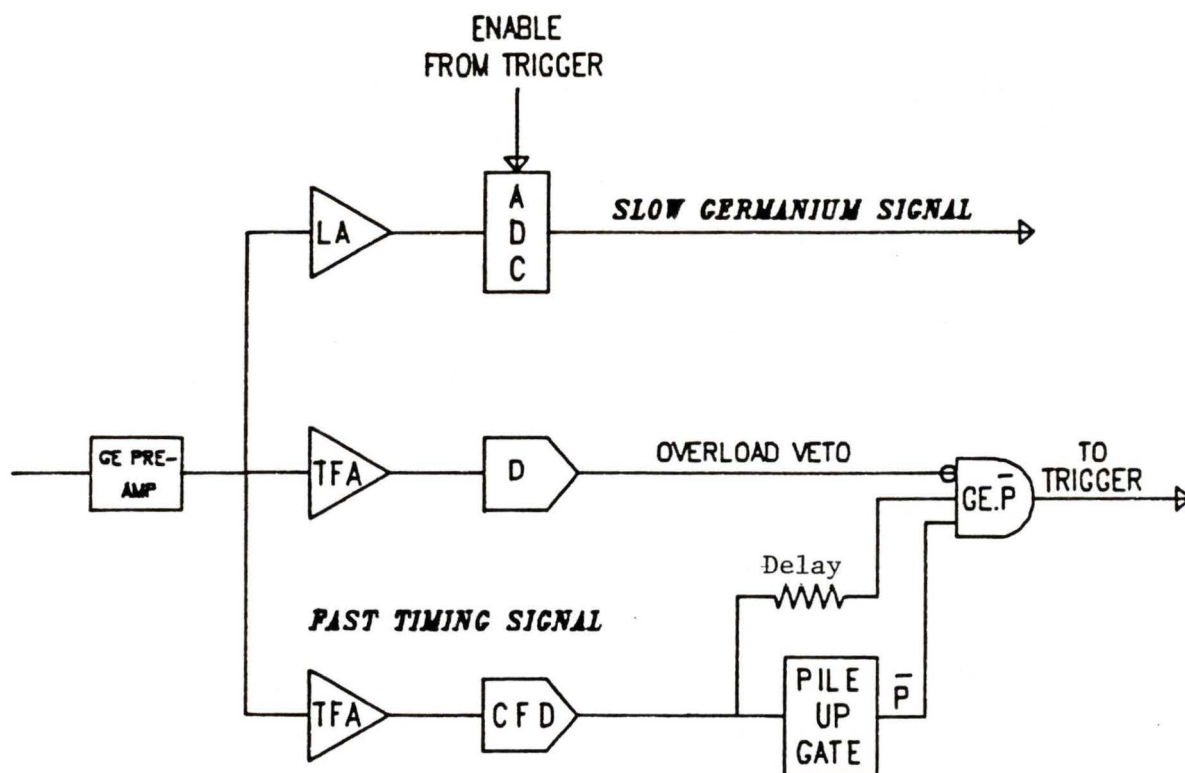


Figure 6: The Germanium Logic.

A fast germanium timing signal was obtained by passing the Ge signal from the pre-amp output through a timing filter amplifier (TFA), where it was differentiated and amplified, and then to a constant fraction discriminator (CFD) which produced a fast signal whose timing was nearly independent of the energy of the input signal. The fast signal was then checked for pile up and was rejected if it followed a previous pulse within the recovery time of the system. The germanium

signal was also passed through another timing filter amplifier and then a discriminator with a high threshold (D). Any signal out from this was used as a veto of the Ge trigger signal for overload rejection.

The germanium pre-amp signal was also shaped and amplified in a linear amplifier and fed into an analogue-to-digital (ADC) converter, where its energy dependent amplitude was converted to a digital code suitable for recording. The ADC was enabled only if all the other logic conditions were met.

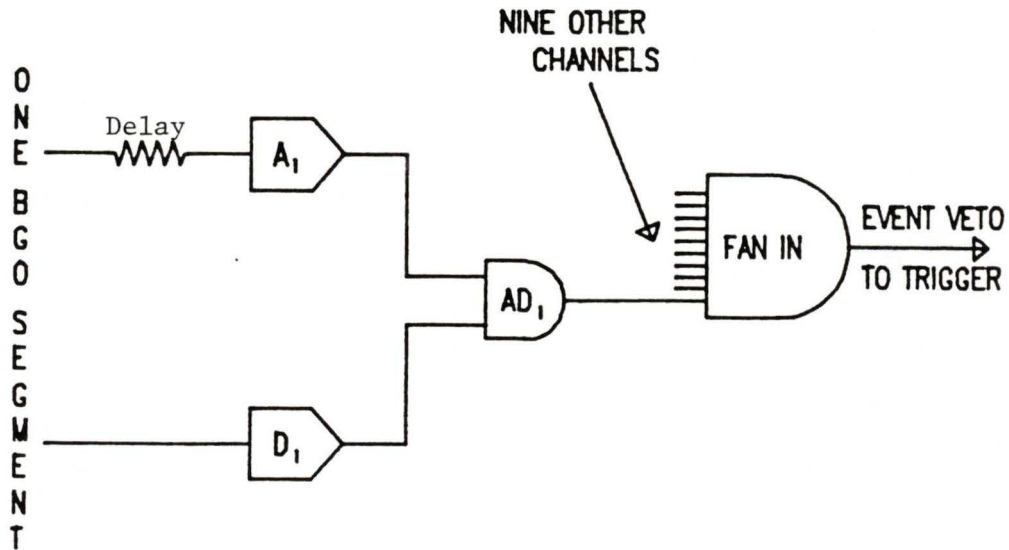
BGO Logic.

Figure 7. The BGO Logic.

The BGO logic was duplicated for each of the ten segments as shown in Figure 7. For each phototube a coincidence was required between the output of the dynode discriminator (D) and the suitably delayed anode discriminator (A). Such a coincidence defined an event in the BGO. (See Chapter 4.)

Trigger Logic.

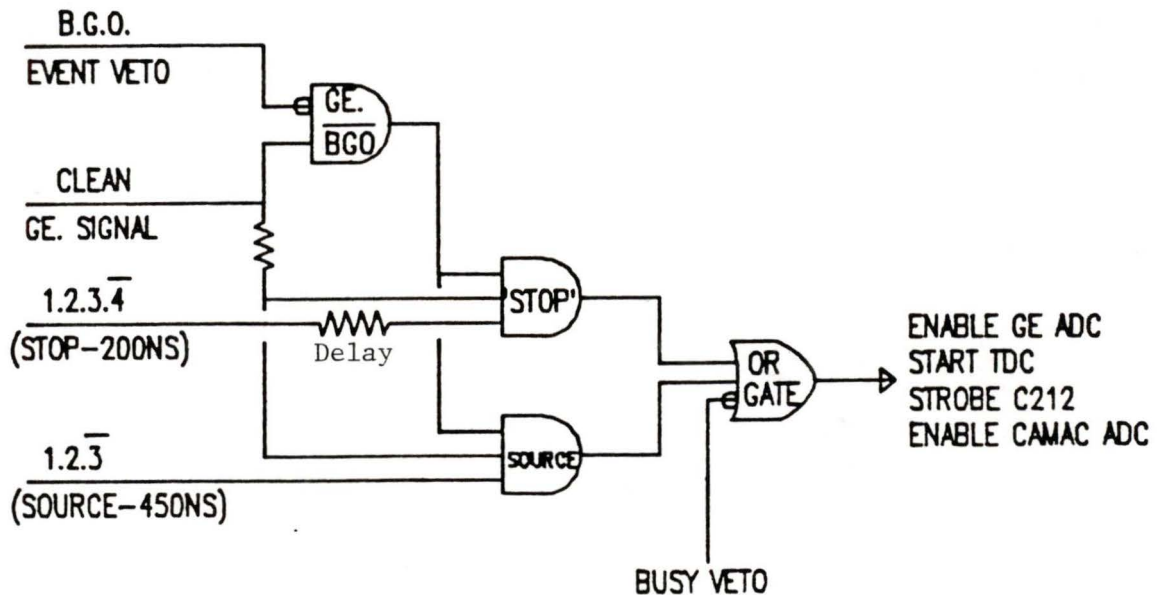


Figure 8: The Trigger Logic.

A non-Compton event was defined in the Ge crystal by an anti-coincidence between a "no-pile-up" fast germanium signal and a BGO event. In turn, this signal, suitably delayed, was in coincidence with a stop signal, or a source event signal, from the telescope logic, a trigger was formed. (In fact some data was taken which didn't require the BGO anticoincidence in order to measure the suppression factor of the suppression system. See Chapter 4.)

Once a trigger was formed it was used for a number of purposes. It was used to gate the ADC, starting the digital conversion of the slow Ge signal. It was also used to strobe the C212 pattern register unit that recorded the characteristics of the events such as

whether it was a stop or a source event. For all events the trigger started a time-to-digital (TDC) converter, which was stopped by the fast germanium signal. This allowed a timing spectrum to be acquired, which showed the time of the event in the Ge with respect to the time of the stop. The timing spectrum could then be used to separate prompt from delayed events. The trigger was also sent to the computer interface (CAMAC) ADC gate and enabled the computer to accept an event. If the computer was busy the trigger was vetoed.

All events within a 200 ns window after a pion stop, or in a 450 ns window after a source type event, were recorded. In order to test the performance of the suppression system, the suppressor veto was removed from the trigger for some runs. The data was then histogrammed with and without a software veto and the background reduction measured. In general, each event written on tape was characterised by six words consisting of the C212 bit pattern, the energy, the time of the stop, the time of a corresponding event in the BGO, the energy in the BGO, and a source flag. In addition, eighteen scalers were recorded representing stops in the target and degrader, anode-dynode coincidences in individual BGO segments, the number of triggers, and a clock so that rates could be calculated.

The complete electronics is illustrated in Figure 9.

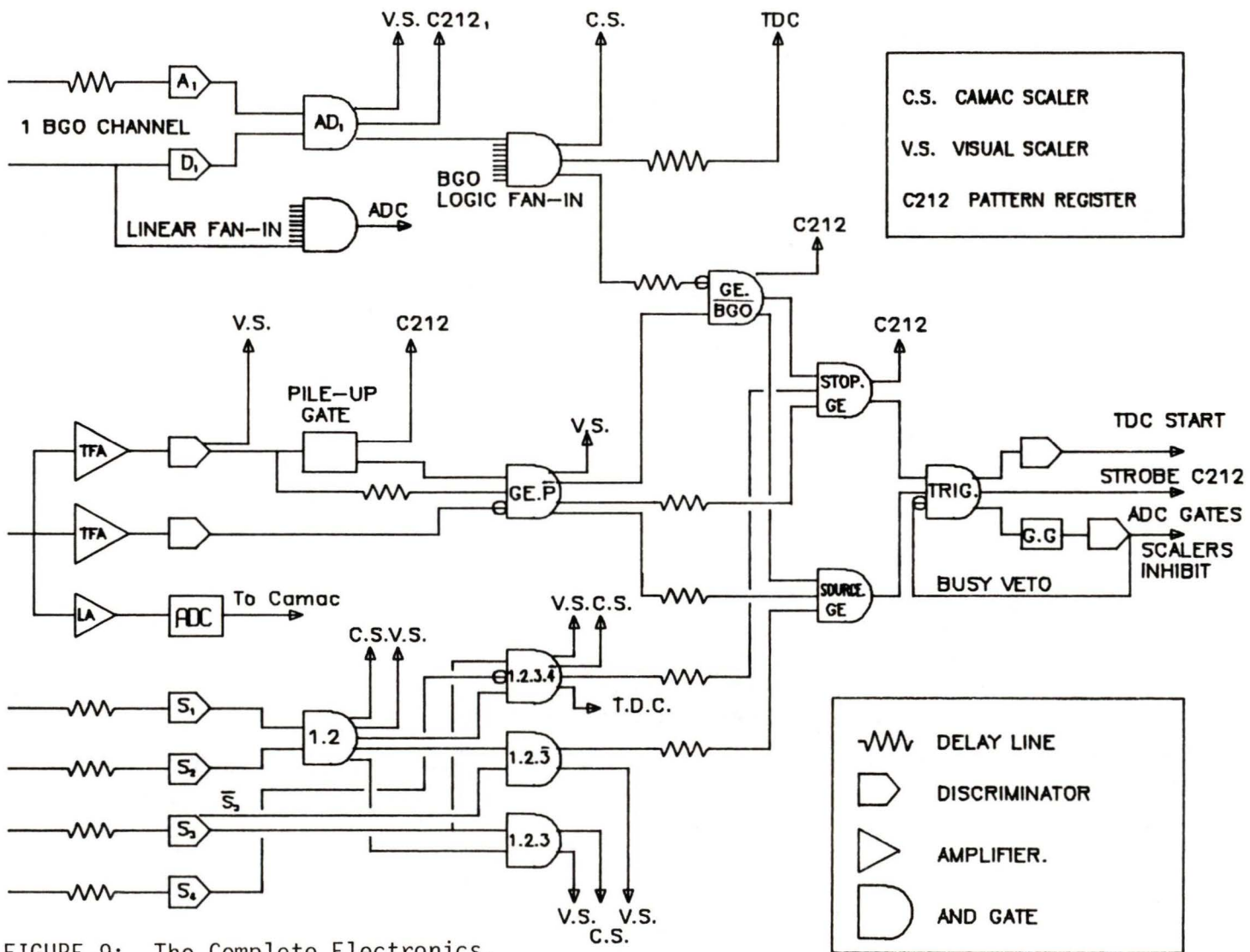


FIGURE 9: The Complete Electronics.

CHAPTER 4: THE COMPTON SUPPRESSION SYSTEM.

Introduction.

When photons impinge on matter, for example on the Ge detector, they interact by three basic processes:

- 1) The photoelectric effect, where the entire energy of the photon is absorbed by a bound atomic electron and reappears as the kinetic energy of that electron as it is ejected, and in the X-ray or Auger electron emitted by the residual ion.
- 2) Compton scattering, where a free electron in the detector acquires a fraction of the incident photon's energy whilst scattering the photon.
- 3) Pair production, where the photon produces an electron-positron pair.

The third effect obviously has a threshold of $2M_e c^2$ (1.02 MeV) and since the X-ray being studied is at 276 keV, this is above the energy region of interest. However, the positron eventually annihilates with the emission of a back-to-back pair of 511 keV photons that produce a clear signature in our spectra. Compton scattering exhibits an almost $1/E$ dependence from 0.1 to several MeV. At low energies, below 0.1 MeV, the dominant mechanism is the photoelectric effect where absorption varies as approximately $Z^5/E^{3.5}$. (Figure 10.)

In reference to the present experiment, a pion stop produces many excited nuclear states that decay with gamma rays with energies in

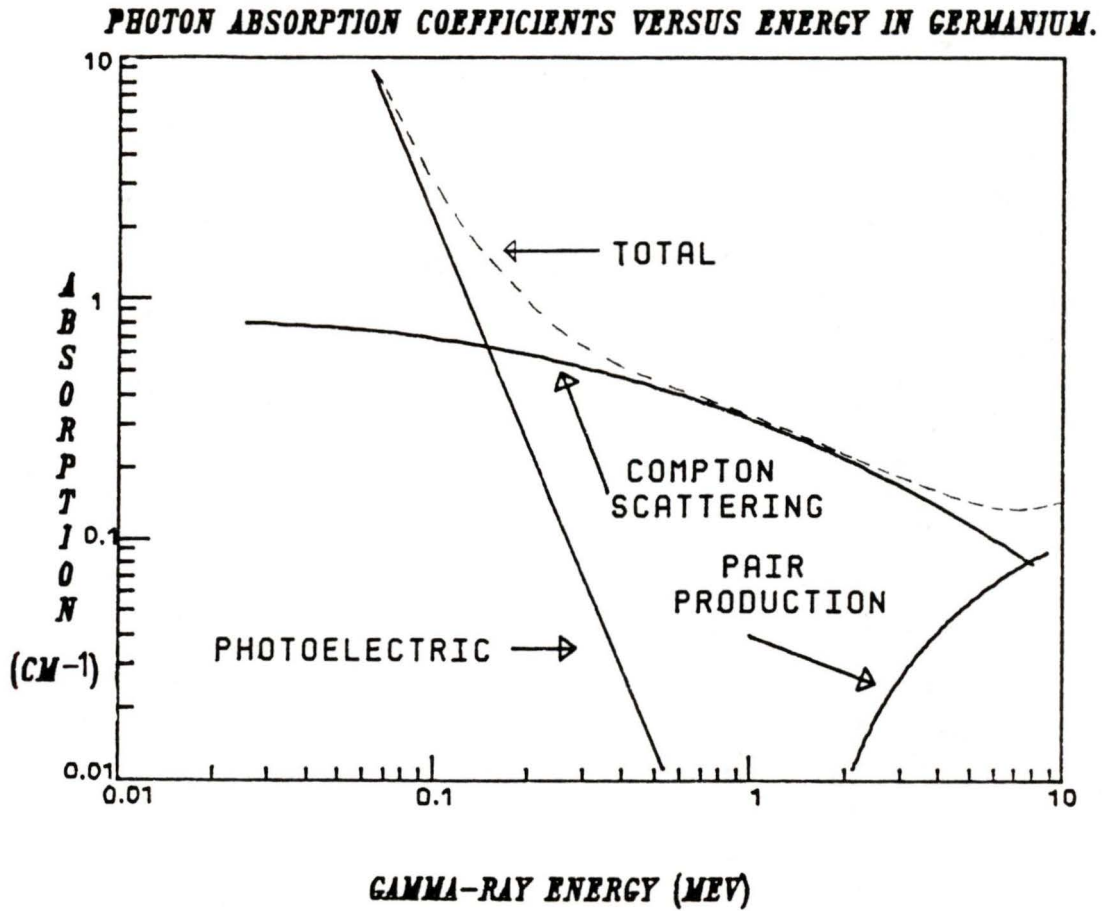


Figure 10.

the few MeV range. Consequently, the most important background is due to Compton scattering. The intensity of photons scattered into a solid angle $d\Omega$ is given to a good approximation by the following form of the Klein-Nishina formula [ST75]:

$$\frac{d\sigma}{d\Omega_{\theta}} = \frac{e^4}{2m^2c^4} \left\{ \frac{(1+\cos^2\theta)}{[1+\alpha(1-\cos\theta)]^2} \right\} \left\{ 1 + \frac{\alpha^2(1-\cos\theta)^2}{[1+\cos^2\theta][1+\alpha(1-\cos\theta)]} \right\} \quad (28)$$

where $\alpha = h\nu/mc^2$, and has a numerical value between 1 and 5 for

incident energies of a few MeV.

The distribution described by this equation is peaked in the forward direction, as can be seen in Figure 11.

ANGULAR DISTRIBUTION OF COMPTON SCATTERING

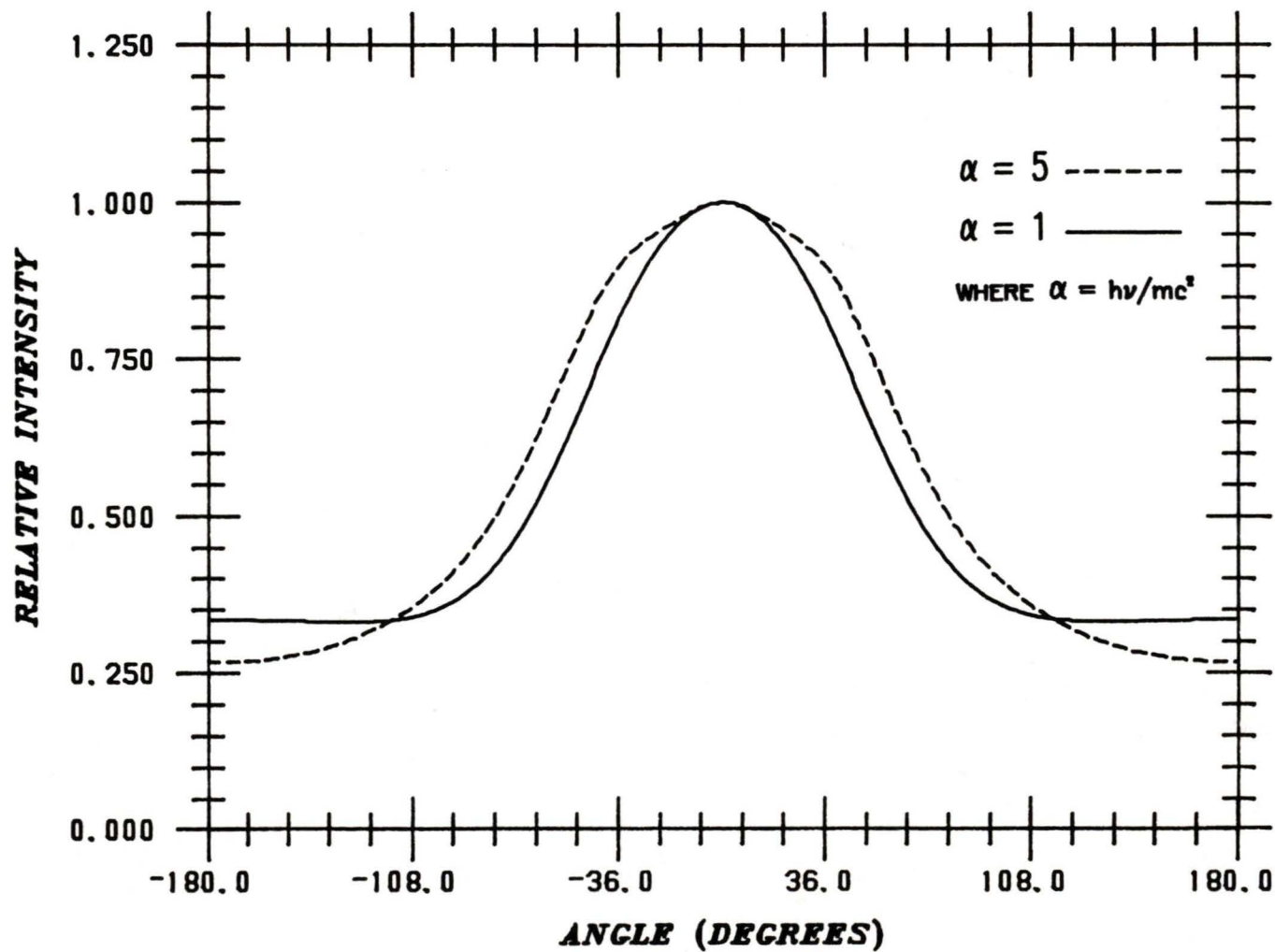


FIGURE 11.

Principle of the Suppression System.

The principle for suppressing such a background is straightforward. One simply detects the photons that are Compton scattered out of the main detector and uses this signal to veto the related event in the central detector.

The first practical suppressors consisted of a Ge detector surrounded by NaI(Tl) scintillator. The disadvantages of this type were that large volumes of the scintillator were required for efficient absorption, and their usefulness in intense-beam environments were restricted by the large $^{127}\text{I}(n,n')$ cross-section.

The present instrument uses bismuth germanate as the scintillator which is much more compact, and so easier to position and shield. In addition, it has a much lower (n,n') cross-section relative to the gamma ray detection efficiency, and the $\text{Ge}(n,n')$ gammas are already present from the germanium in the main detector. The main disadvantage of BGO is its low light yield, but this was partly compensated for in the design.

Construction of the Suppressor.

The spectrometer is constructed (OL84) out of sixteen $5.5 \times 5.5 \times 8.0$ cm BGO crystals, arranged as four pairs in either half of an aluminium shell. (See Figure 12.) At one end is the hole for the incoming photons, and perpendicular to this is the entrance hole for the snout of the Ge detector, so that the forward scattered photons can best be detected.

Each pair of crystals is optically coupled together but isolated from all the rest, and viewed from one end by a 5 cm phototube. However, the front pair of crystals in each half is viewed from both ends since the constriction due to the holes resulted in an 80% attenuation of the signal from one end to the other, in contrast to 10% in the other pairs.

The phototubes and their associated bases, preamplifiers, and magnetic shielding, are mounted in a light-tight enclosure.

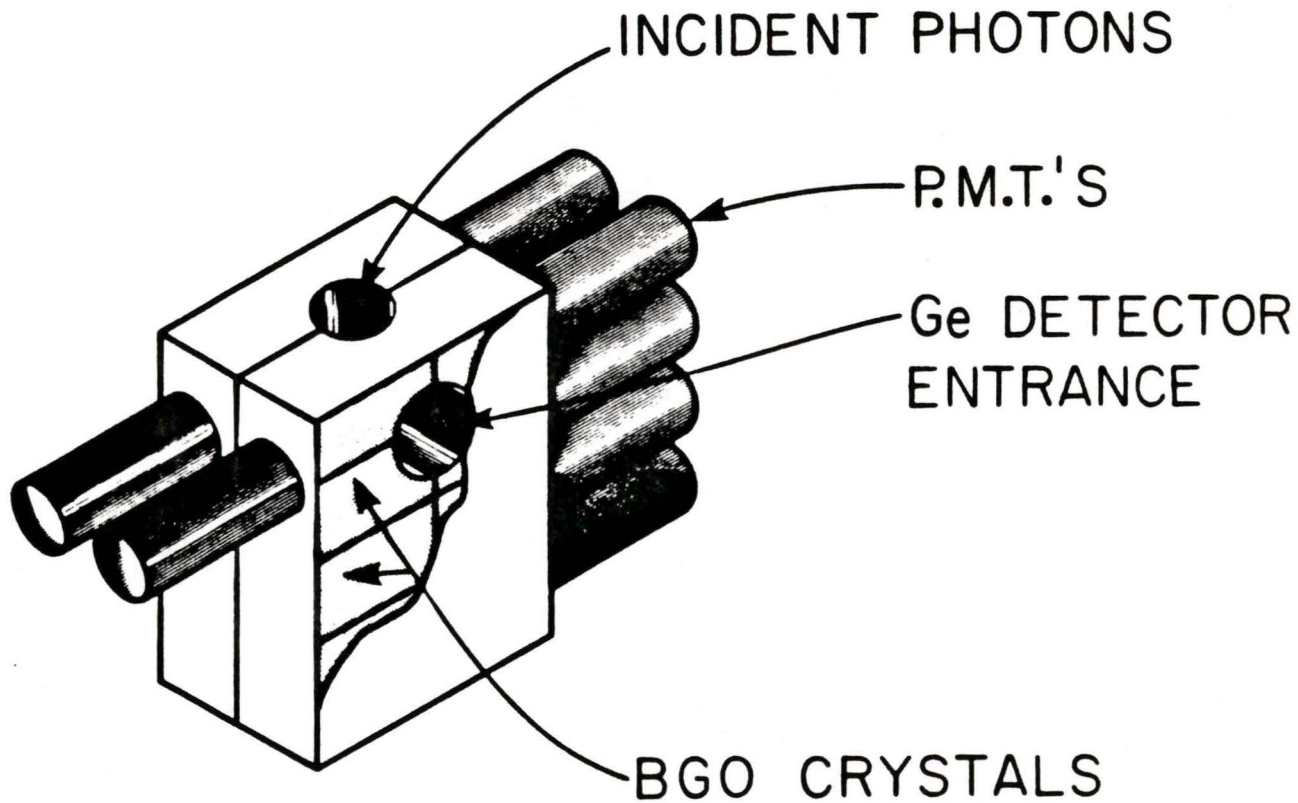


FIGURE 12: Schematic of the Compton Suppression Spectrometer.

Operation of the Suppressor.

Since the bismuth germanate has a relatively low light yield, it is necessary to work in the single photo-electron mode in order to obtain a reasonable low energy threshold. To achieve this, low noise amplifiers were mounted directly on the tube bases. The operating philosophy was to use the anode signal for timing and a shaped dynode signal for energy resolution and discrimination. A valid event in a particular segment is defined by an anode-dynode coincidence. Each of the ten segments was instrumented separately to allow high rate capabilities for in-beam use. In practice, a total rate of 200 Hz did not result in a single segment rate exceeding 50 Hz.

With a typical 1900 volts on the phototube, the amplifier on the anode provided a timing signal of 70 mV, and the dynode amplifier, which shaped the pulse for energy resolution, was about 50 mV. The R.M.S. noise level was less than 5 mV. The anode signal was passed to a burst guard (time-over-threshold) type discriminator, which provided an output pulse corresponding to the length of time the input signal was over the threshold. For a single photoelectron this gave approximately a 10 ns pulse, and for a large signal this would extend up to about 500 ns. (See Figures 13 and 14.)

The dynode signal, generated by an up-date type discriminator, was set to 80 ns, which corresponded to the maximum timing jitter that would occur between the anode and dynode signals. A signal from a single photoelectron of about 50 keV has a decay time of about 300 ns

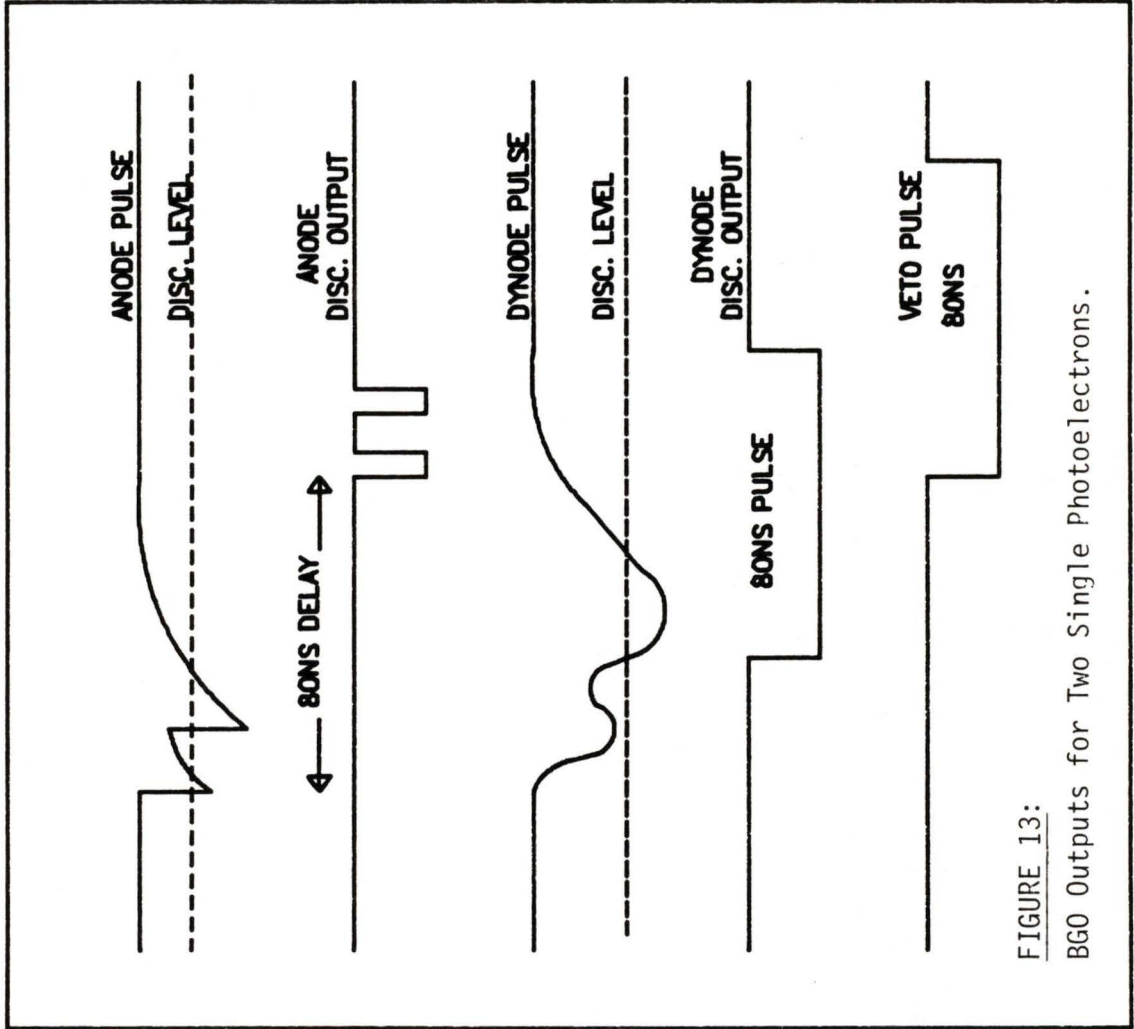
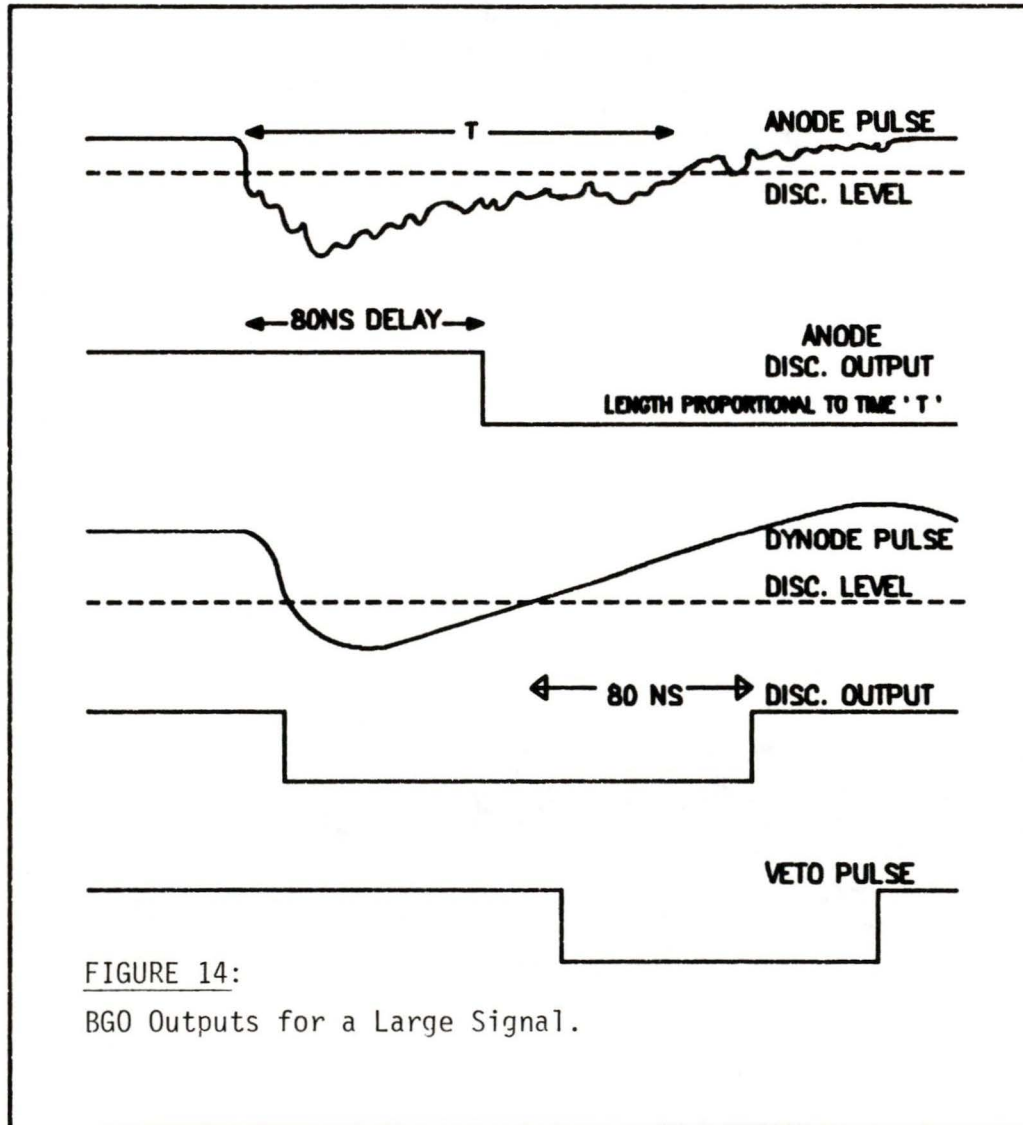


FIGURE 13:
BGO Outputs for Two Single Photoelectrons.



in BGO, so the dynode discriminator was set such that it required two single photoelectrons within 80 ns, to fire. This had two consequences: Firstly, it meant that single photoelectrons would not fire the dynode, and shut the channel down for 80 ns. Secondly, because the dynode amplifier pulse would overshoot when recovering, this suppressed refiring on the last few photons following a big pulse. Again this reduces unnecessary deadtime.

The anode signal was delayed until nearly the end of the dynode signal, and then if there was a coincidence, an 80 ns veto pulse was formed.

Performance of the Suppression System.

The suppression of the Compton background obtained from the system is characterised in terms of the peak-to-total count ratios in the suppressed and unsuppressed data, Q_s and Q_u , respectively. The suppression factor, 'S', that is used in Monte-Carlo calculations is given by:

$$S = (1/Q_u - 1) / (1/Q_s - 1) \quad (29)$$

However, for practical purposes the suppression factor is usually defined as just the ratio of unsuppressed to suppressed data. This convention is followed from here on.

Using a ^{60}Co source, the spectrum in Figure 15 was obtained. This shows an average suppression of the background by about 4.0 times, although the suppression was considerably better than this over much of the spectrum. The reason for this can be seen to be due to the Compton edges in the unsuppressed data which appear as broad peaks in the suppressed data. These correspond to photons that are scattered back out of the entrance hole, and thus not detected. This effect was important when fitting the Compton edge of the $\text{Na } 440\gamma$, that lies under the $\pi\text{-Na}(2-1)$ X-ray. Only about 5% of the photopeak counts were vetoed by the suppressor.

The in-beam performance was investigated using a beam of $2 \times 10^5 \pi^-/\text{sec}$ from the TRIUMF M13 pion channel, stopping in a 50 g target of sodium hydride. The complete experimental set up is described in Chapter 3. All events within a 200 ns window of a stop in the

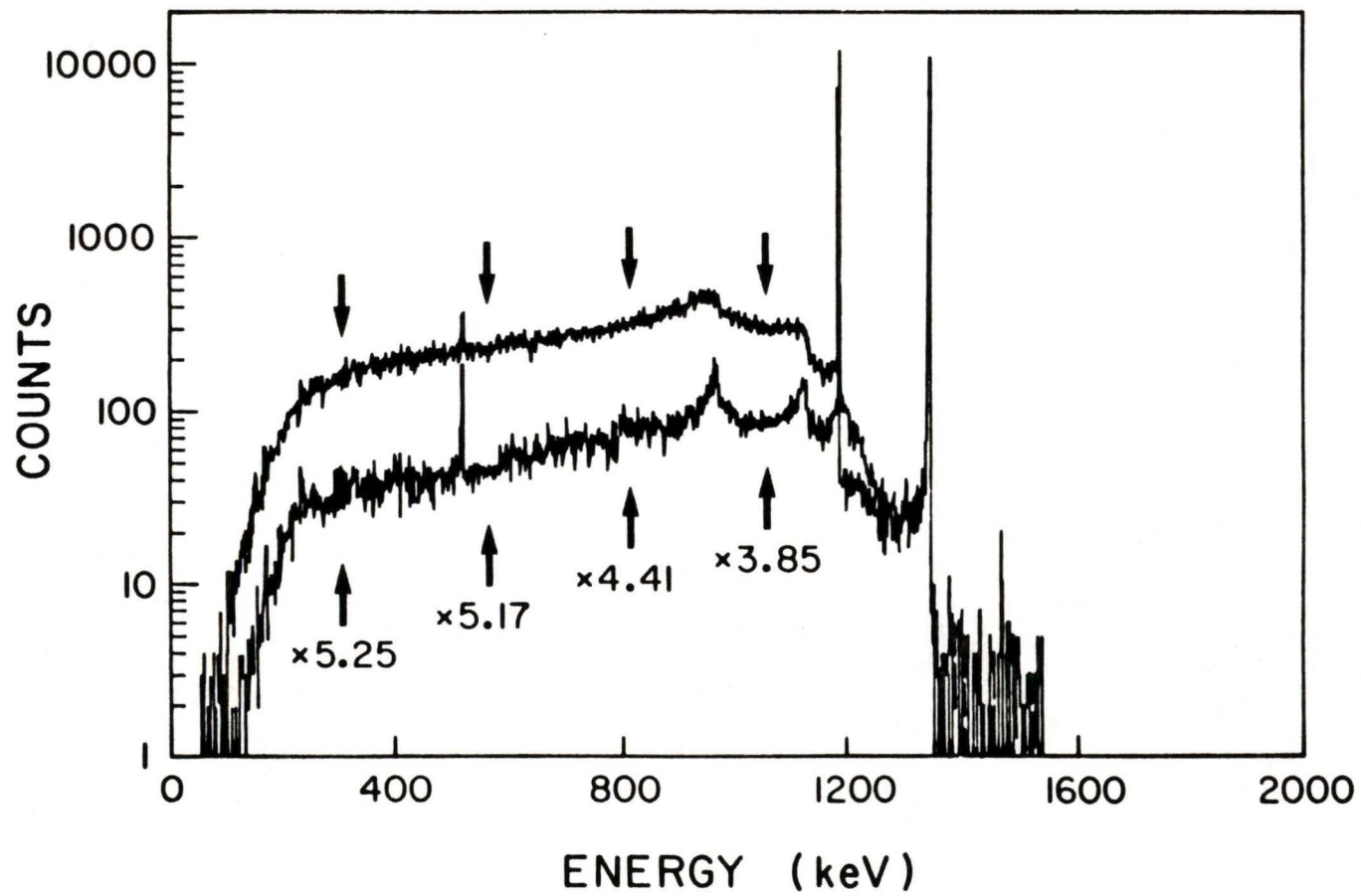


FIGURE 15: Suppressed and Unsuppressed ^{60}Co Spectra.

target, or within 450 ns of a stop in the degrader, were recorded. The latter allowed a calibration source spectrum to be obtained from adjacent gamma sources, under in-beam conditions. (The degrader was well shielded from the detector.) A prompt software window of 7 ns was defined, dividing the stop spectrum into 'prompt' and 'delayed' data.

Figure 16 shows the prompt suppressed and unsuppressed spectra. The suppression obtained at lower energies is comparable to the out-of-beam data of Figure 15, exhibiting a reduction in the background of five or six times around the sodium X-ray, at 276 keV. The suppression improves up to about 900 keV. Figure 17 shows the data that was actually removed from the unsuppressed spectrum by the suppressor. The large peak shows that a substantial proportion of the 511 gamma rays from pair production are suppressed, in addition to the continuum Compton background. The small peaks (for example, the one labelled 'A' in Figure 17) show that fewer than 5% of the photopeak counts were suppressed by random coincidences.

Figure 18 shows the suppressed and unsuppressed delayed spectra. Here the suppression is markedly better than in the prompt spectrum. The dominant gammas in the delayed spectrum come from (n,n') interactions in the germanium, which are largely excluded from the prompt spectrum by a fairly sharp timing cut. The improvement in the suppression is most likely due to veto signals in the BGO produced by the scattered neutrons. This is supported by the fact that the corresponding photopeak intensities are reduced to half by the suppressor.

Figure 19 shows a source spectrum acquired under in-beam conditions as described above.

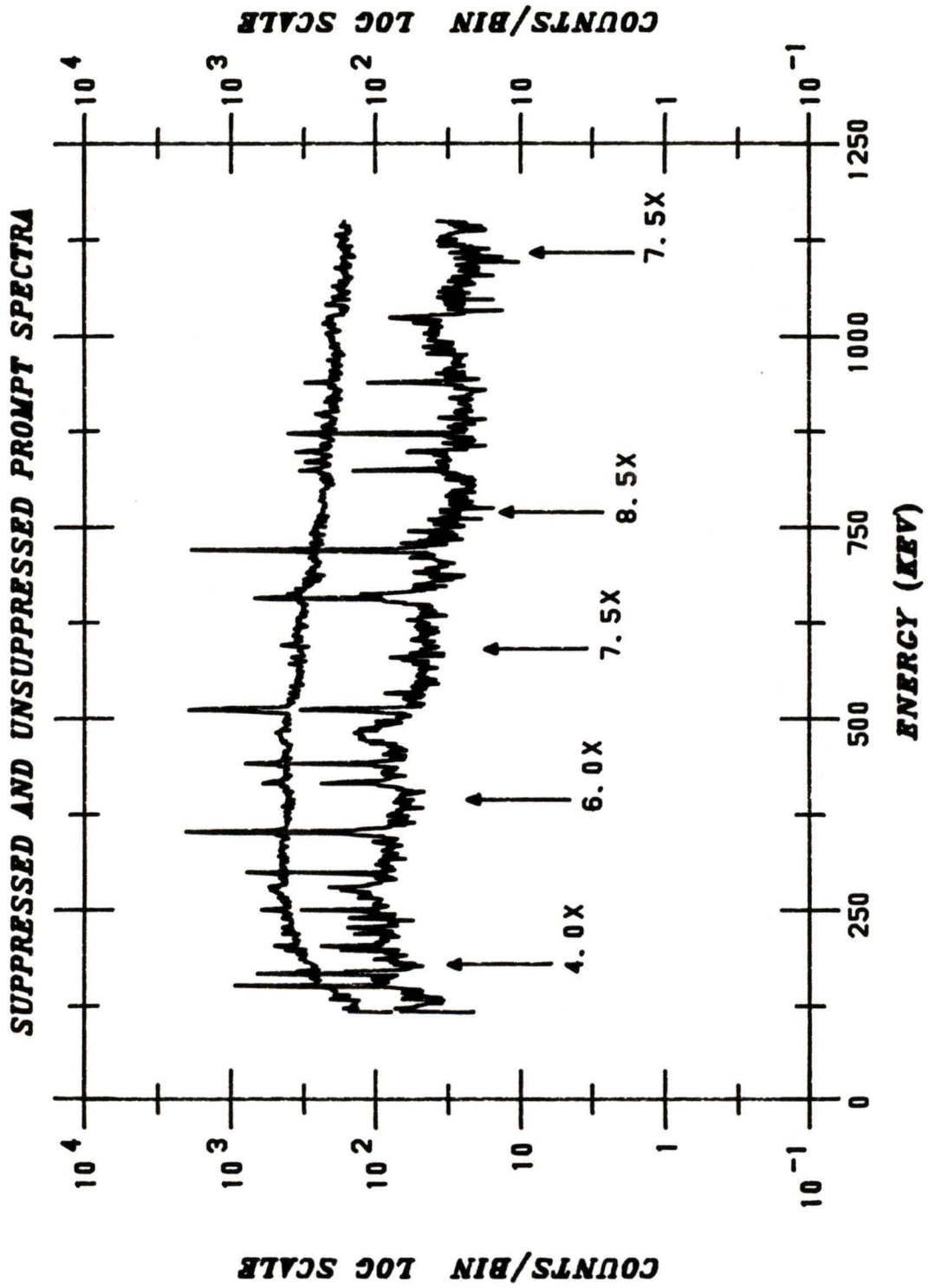


FIGURE 16.

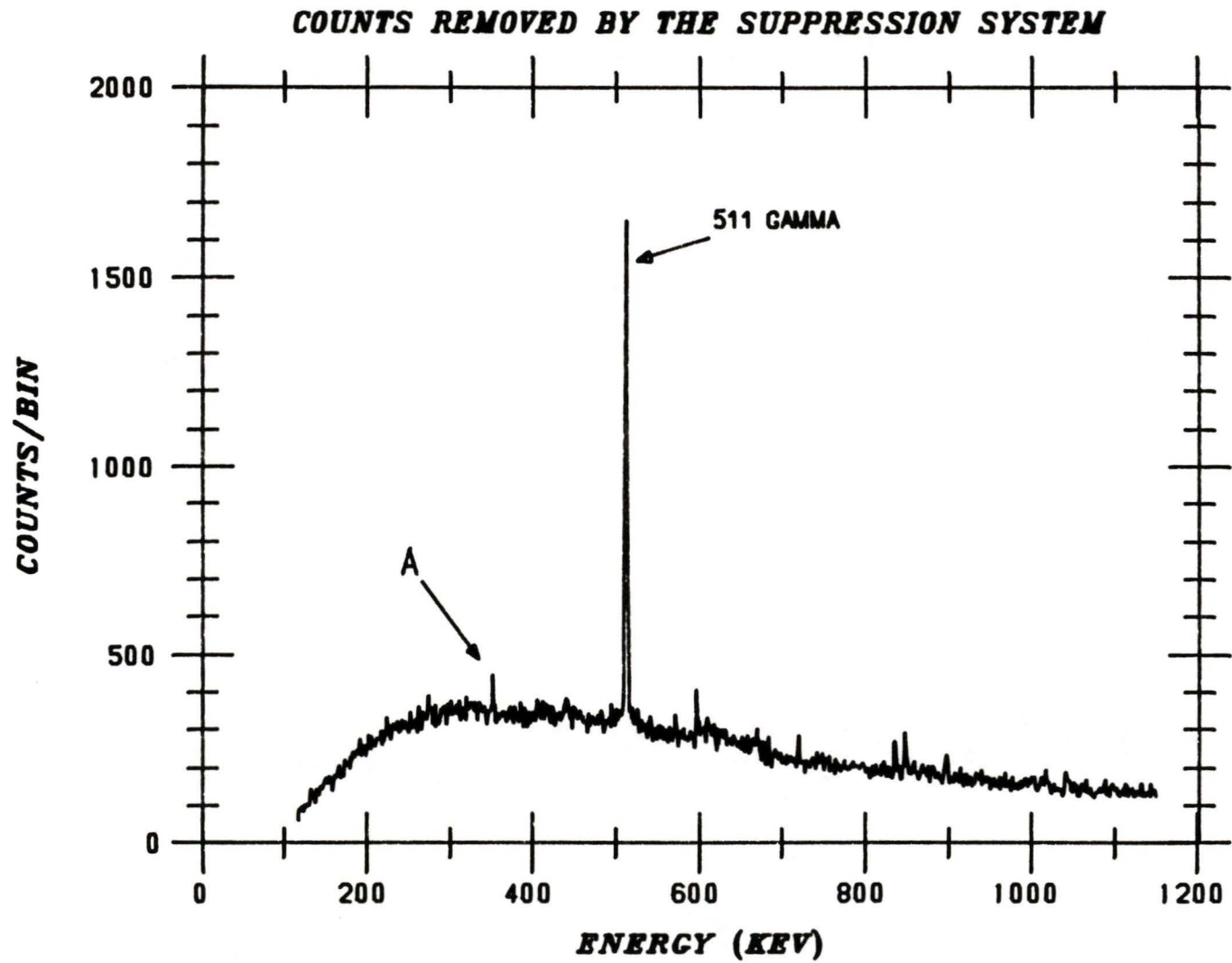


FIGURE 17:

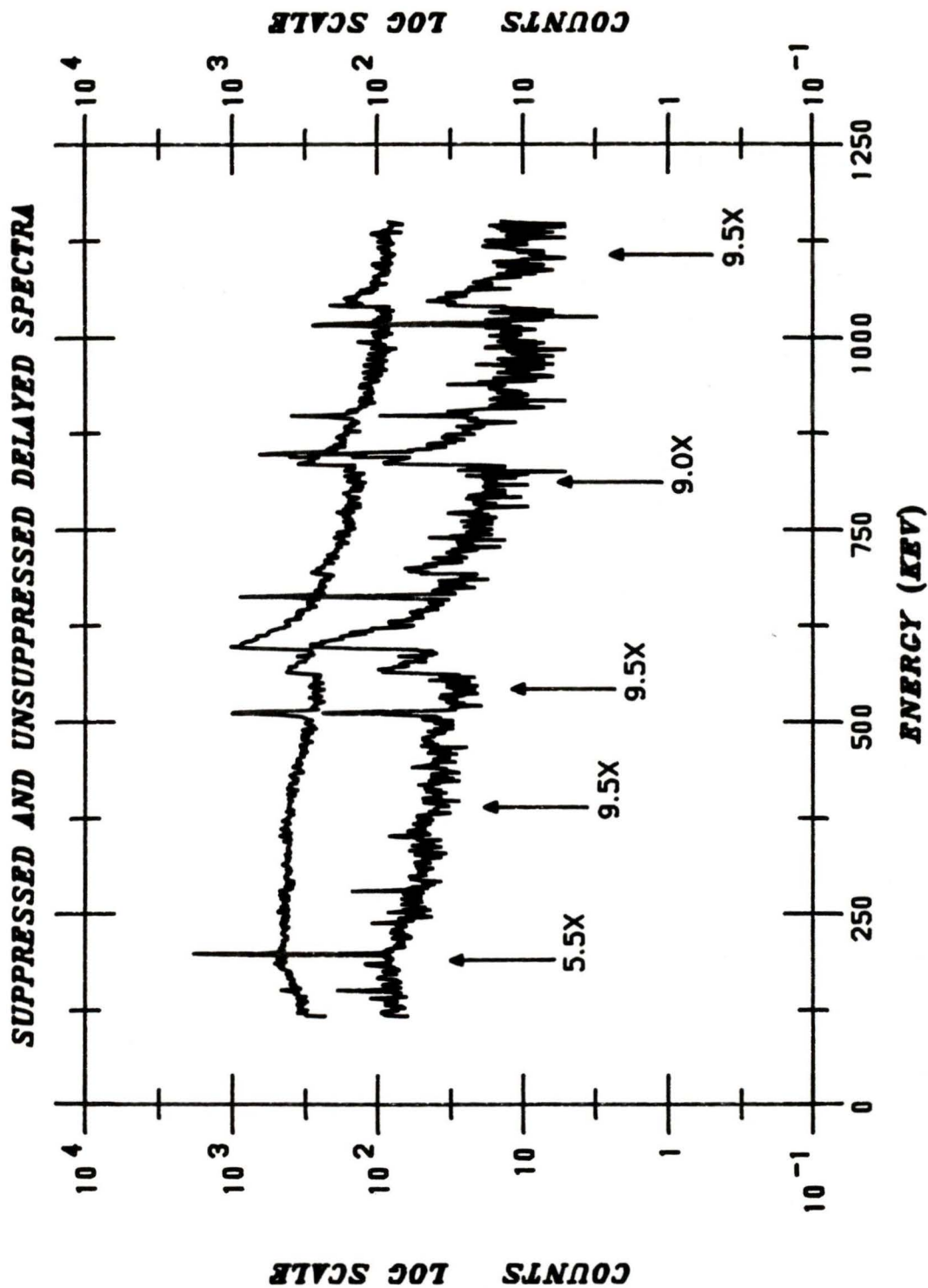


FIGURE 18.

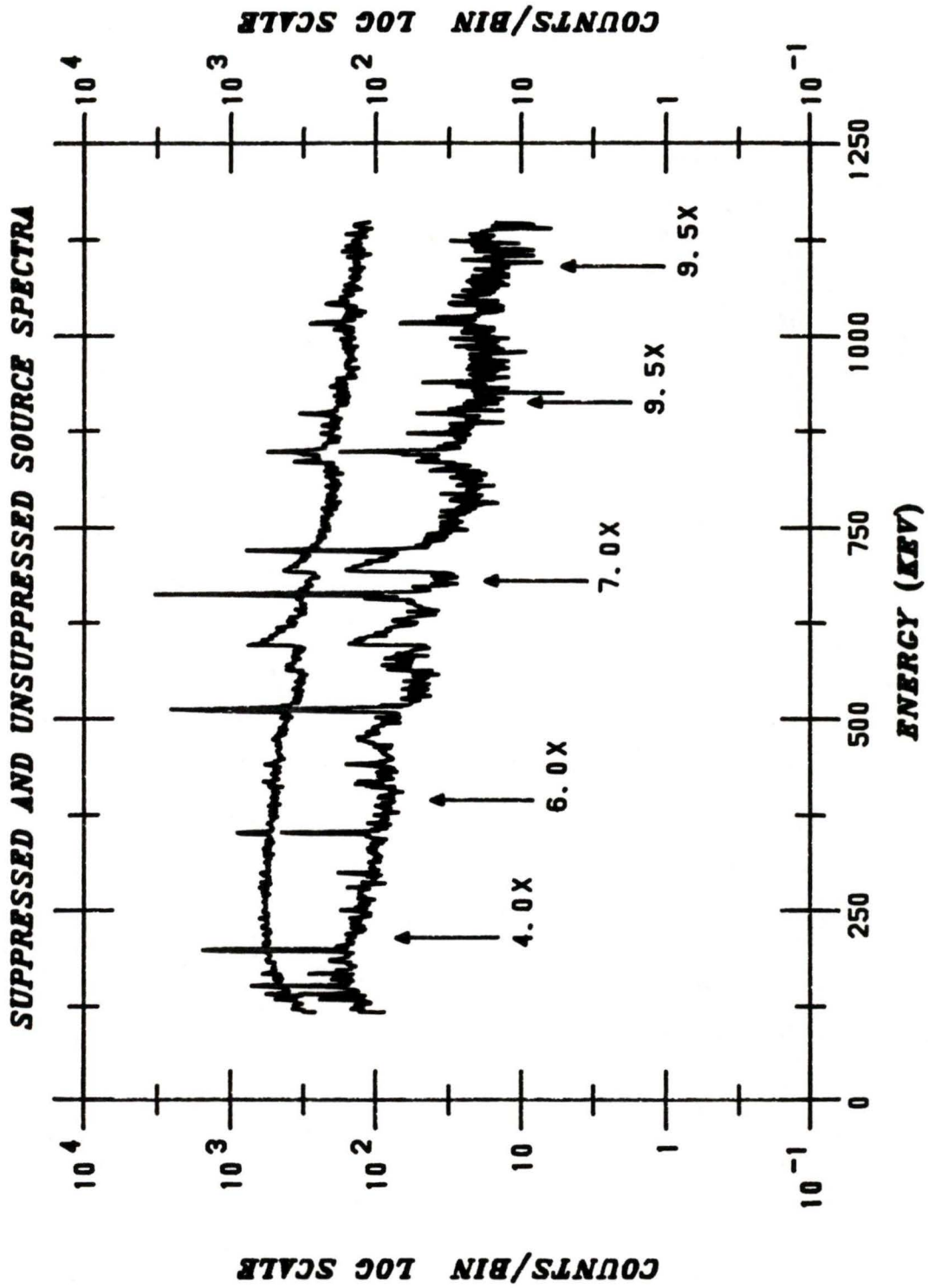


FIGURE 19.

Conclusion.

The performance of the BGO Compton suppression system falls somewhat below that of the best NaI(Tl) devices, where a maximum reduction in background of about 14 times, has been reported (BE77). However, the bismuth germanate system was indispensable in the present experiment because a NaI system would have introduced many more counts into the sodium 440 keV gamma's Compton edge, which lies right under the X-ray that was to be measured.

Monte-Carlo calculations (HA83) predicted that a suppression factor of about eleven should be possible with sources out-of-beam for 1 MeV photons, whereas the best observed factor was between five and six. However, the calculations did not account for dead layers of material between the central detector and the suppressor, nor inactive layers in the detector core. The suppressor could be improved by increased segmentation, particularly of the front pairs of crystals, and a central detector with a minimum of dead layers would be beneficial.

In practice, the suppressor has reduced backgrounds sufficiently to observe very weak broadened pionic X-ray transitions, and in particular, has made possible a new and rather different measurement of the seemingly anomalous sodium 2-1 X-ray.

CHAPTER 5: THE ANALYSIS.

Introduction.

The data recorded on tape during this experiment included three spectra: a timing spectrum, an energy spectrum associated with a π -stop, and an energy spectrum of 'in-beam condition' source events. By forming a scatterplot of energy versus the timing information, a fairly tight timing cut was placed on the π -stop spectrum to reduce backgrounds. This resulted in a prompt spectrum, which contained the sodium 2-1 pionic X-ray, and a delayed gamma spectrum. The goal of the analysis was to find the energy and width of the X-ray.

The delayed and source spectra were used to obtain information on detector resolution and "tailing", and well determined peaks in all three were used for the energy calibration. ^{75}Se and ^{133}Ba source spectra were also recorded out-of-beam for information on detector efficiency, and an activated gold source was used to facilitate fitting the Compton edge of the sodium 440 keV gamma.

The Peak Fitting Program JAGSPOT.

The data analysis was performed using a gamma ray fitting program called JAGSPOT. The program, originally from Chalk River, was developed for use at the University of Victoria by Dr A. Olin (OL78b), to fit Lorentzian broadened pionic X-rays.

The experimental spectrum of length i channels, up to 500, is fitted to a function $\phi(x_i, \bar{a})$ where the parameters \bar{a} describe the background, lineshape, peak intensities and tailing. The general form of the fitting function is:-

$$\phi(x_i, \bar{a}) = a_1 + a_2 x_i + b(x_i) + \sum_{j=1}^N a_{2j+3} f_{\alpha j}(x_i - a_{2j+4}) \epsilon(x_i) \quad (30)$$

where $\epsilon(x_i)$ is the detector efficiency at channel x_i , $f_{\alpha N}$ is the lineshape function for the N 'th peak, and $b(x_i)$ is a function describing backgrounds due to tailing.

Up to ten peaks may be fitted simultaneously, either with a Gaussian lineshape, or with the convolution of the Gaussian with one of three Lorentzians. Thus all ten peaks could be pure Gaussian with the same full-width-half-max (FWHM), or any of them may be a Lorentzian broadened peak, with up to three different FWHM widths being possible in the same spectrum.

The background spectrum was generally fitted as having a linear dependence with energy, although the effect of fitting an

exponential background was investigated. In addition, the background contains another term, $b(x_i)$

$$b(x_i) = a_{25} \sum_{j=1}^N (y_j - d_j) e^{-a_{26}(x_j - x_i)} \quad (31)$$

due to the low energy tailing of the detector response; y_j is the number of counts in channel j and d_j is the background. Thus, the background has the overall form:

$$a_1 + a_2 x_i + b(x_i) \quad (32)$$

The detector efficiency was determined as a linear function of energy in the range of interest, by fitting selenium source data. The efficiency was normalised to 1.0 at the center of the fitted window, and the correction was applied only to the lorentzian broadened peaks.

In the latest version of the program it is possible to ignore certain regions within the fitted region. This conveniently removes the problem of trying to fit contaminant peaks whose detailed shape is not relevant to the problem of determining the X-ray width and energy.

The program is run from an input file that contains all the information on the position and amplitude of the peaks, the line shape they are to be fitted with, the resolution, the tailing, and the background. These parameters can either be fixed or allowed to float to obtain the best fit as judged by a minimum in the random variable χ^2 .

Calibration.

Energy calibration was achieved by measuring the best determined X-rays and gamma rays due to stops in the target and from the in-beam source spectrum. The out-of-beam gamma source spectra were not used due to a difference in their offset and because of stabiliser problems associated with them. Table 1 lists the gamma rays and energies used in the calibration. The energies of the gamma rays versus the peak channel numbers were fitted to both a linear and a quadratic function using a least-squares fit. The quadratic term was always small (of the order 10^{-8}) so the linear fit was used (Figure 20). The result was:

$$E = A(1) + A(2)*channels \quad A(1)=0.664 \text{ (3\%)} \\ A(2)=0.14334 \text{ (0.003\%)} \quad (33)$$

This provided a sufficient energy calibration.

Table 1. The calibration peaks.

Peak	Peak Channel	Energy in KeV
π -Cl (3-2)	1045.9 (0.1)	150.55 (0.15)
^{19}F -gamma	1370.76 (0.06)	197.15 (0.01)
μ -Na (2-1)	1740.79 (0.08)	250.21 (0.15)
^{21}F -gamma	1947.77 (0.2)	279.92 (0.06)
^{137}Cs -gamma	4611.37 (0.05)	661.661 (0.003)

FIT OF CALIBRATION DATA

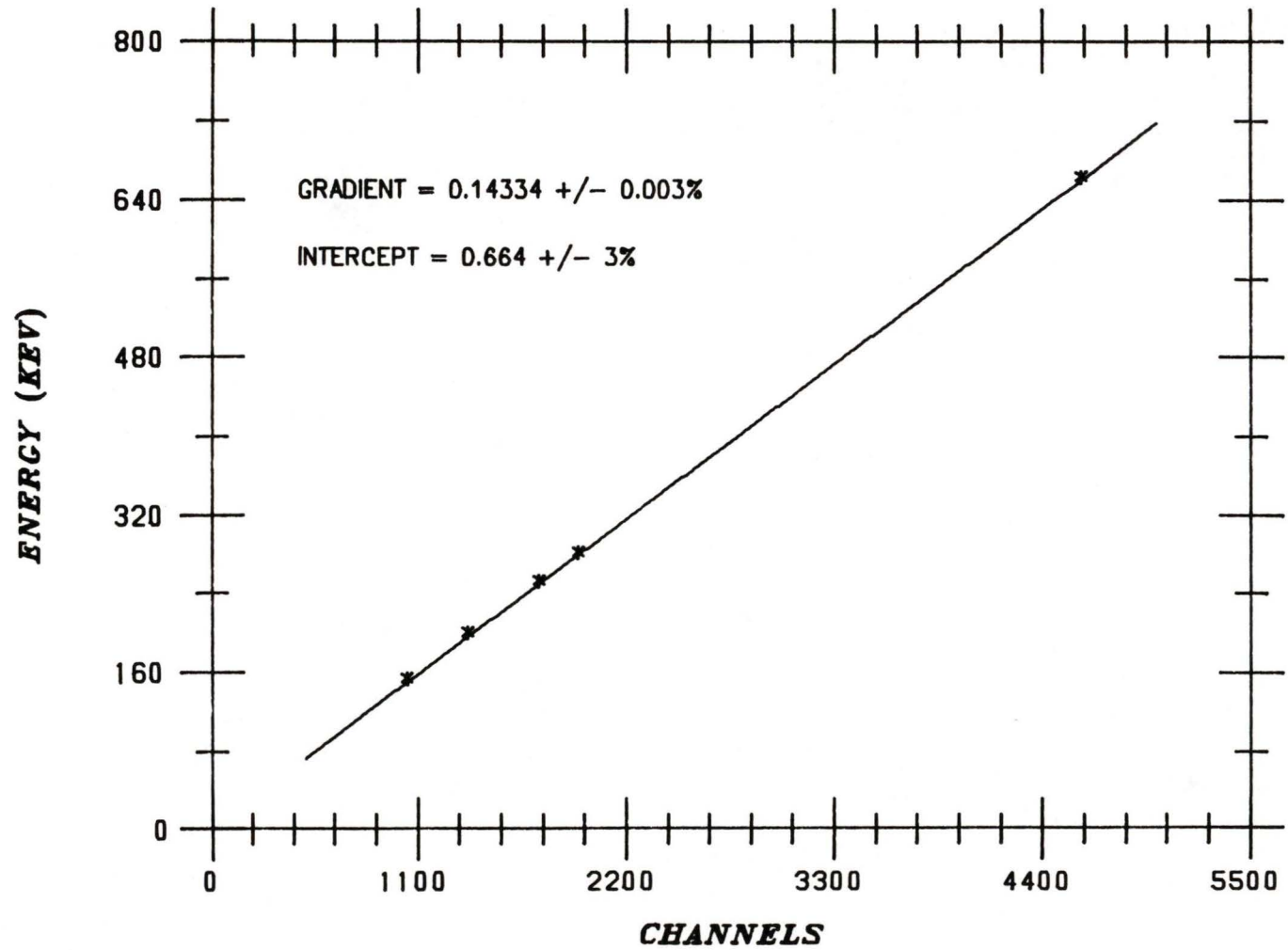


FIGURE 20.

The Detector Response.

The intrinsic detector resolution was determined by fitting as many clean gamma rays as possible in the prompt, delayed, in-beam source, and out-of-beam source spectra (see Figure 21). It is clear that the in-beam resolution is slightly worse than that obtained out-of-beam, as would be expected due to the high rates in the beam environment. A linear fit of the in-beam data was used to determine the FWHM at 276 keV of 1.0(0.1) keV.

In a similar manner, the tailing of the detection system was determined by fitting as many gamma rays as possible with the tailing parameters floating. The values obtained are tabulated in Table 2. The result was a small exponential tail, described by two parameters (EXT1 and EXT2) representing its amplitude and range. Since much of the tailing data was consistent with zero, the uncertainty in the tail was considered to run from zero to the maximum value obtained.

Due to the size of this uncertainty, any energy dependence of the tailing was insignificant. To obtain accurate tailing data, good statistics and a very clean spectrum would be required.

The relative efficiency of the detector over the energy range of the sodium X-ray fits was obtained from the ^{75}Se source spectrum (Figure 22.) Areas of the 5 prominent peaks were measured, and the relative efficiency calculated by comparing these numbers with the carefully measured relative intensities (GE77). A linear fit of the data points was assumed (Figure 23), of the form:

$$\epsilon_i = (1.315 - 0.00121 * E_i) / \phi \quad (34)$$

where ϵ_i is the efficiency at channel i , and ' ϕ ' is the efficiency at the centre channel of the fitted region. A barium spectrum recorded over the same range was not used because of a problem with the stabiliser, or a peculiar effect due to the suppression system.

Table 2. Tailing data.

Gamma Ray	EXT1	EXT2
^{19}F (197 keV)	0.0012 (0.0005)	0.028 (0.011)
^{137}Ba (303 keV)	0.0009 (0.0003)	0.024 (0.02)
^{198}Au (412 keV)	0.0006 (0.0002)	0.030 (0.015)
* ^{198}Au (412 keV)	0.00045 (0.00004)	0.020 (0.003)*

* This was a measurement made with good statistics to examine the gold Compton edge. It also served to provide the most accurate tailing information, and was appropriately weighted. The tailing coefficients from the fitting were:

$$\text{EXT1} = 0.0005 \quad \text{EXT2} = 0.02$$

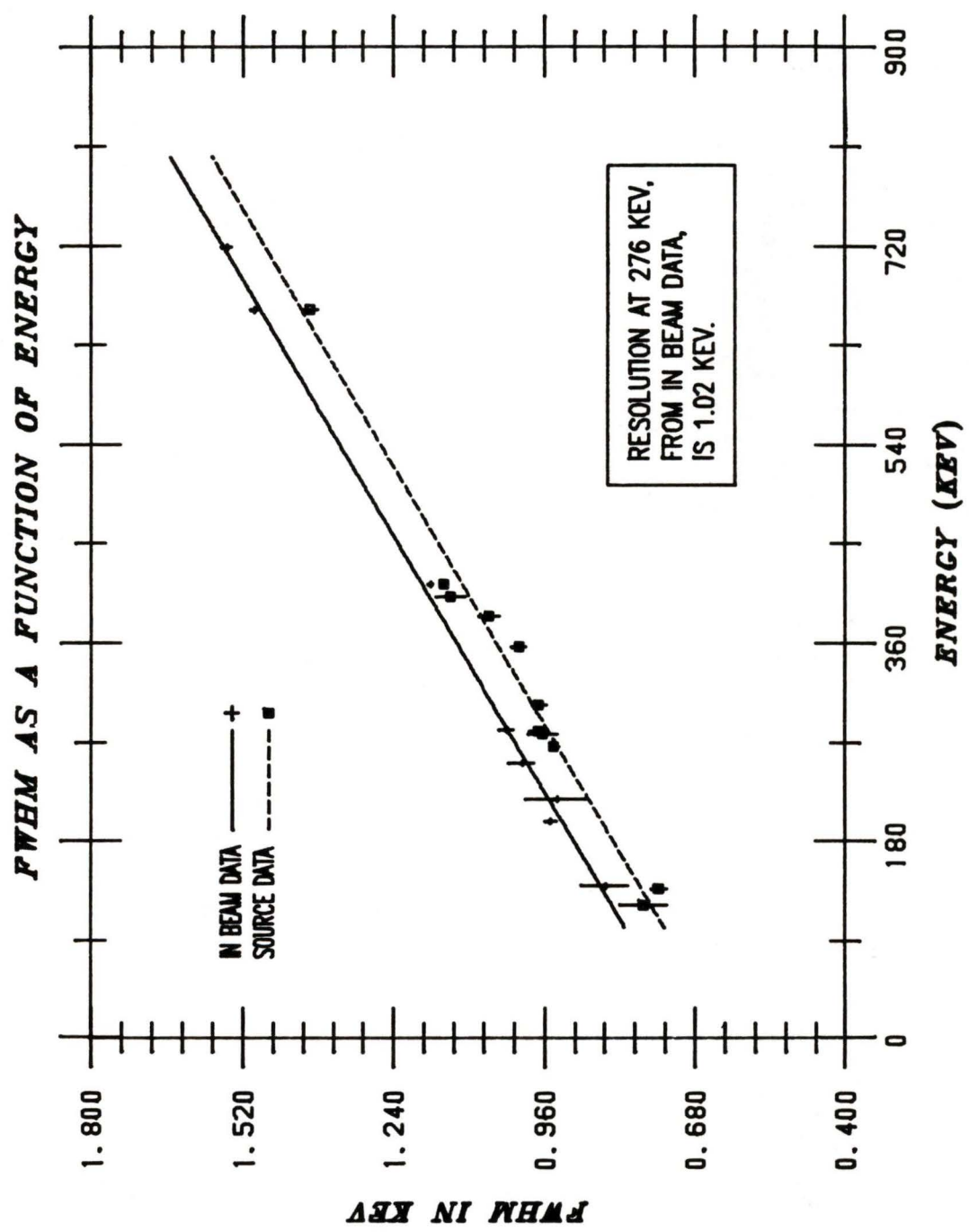


FIGURE 21.

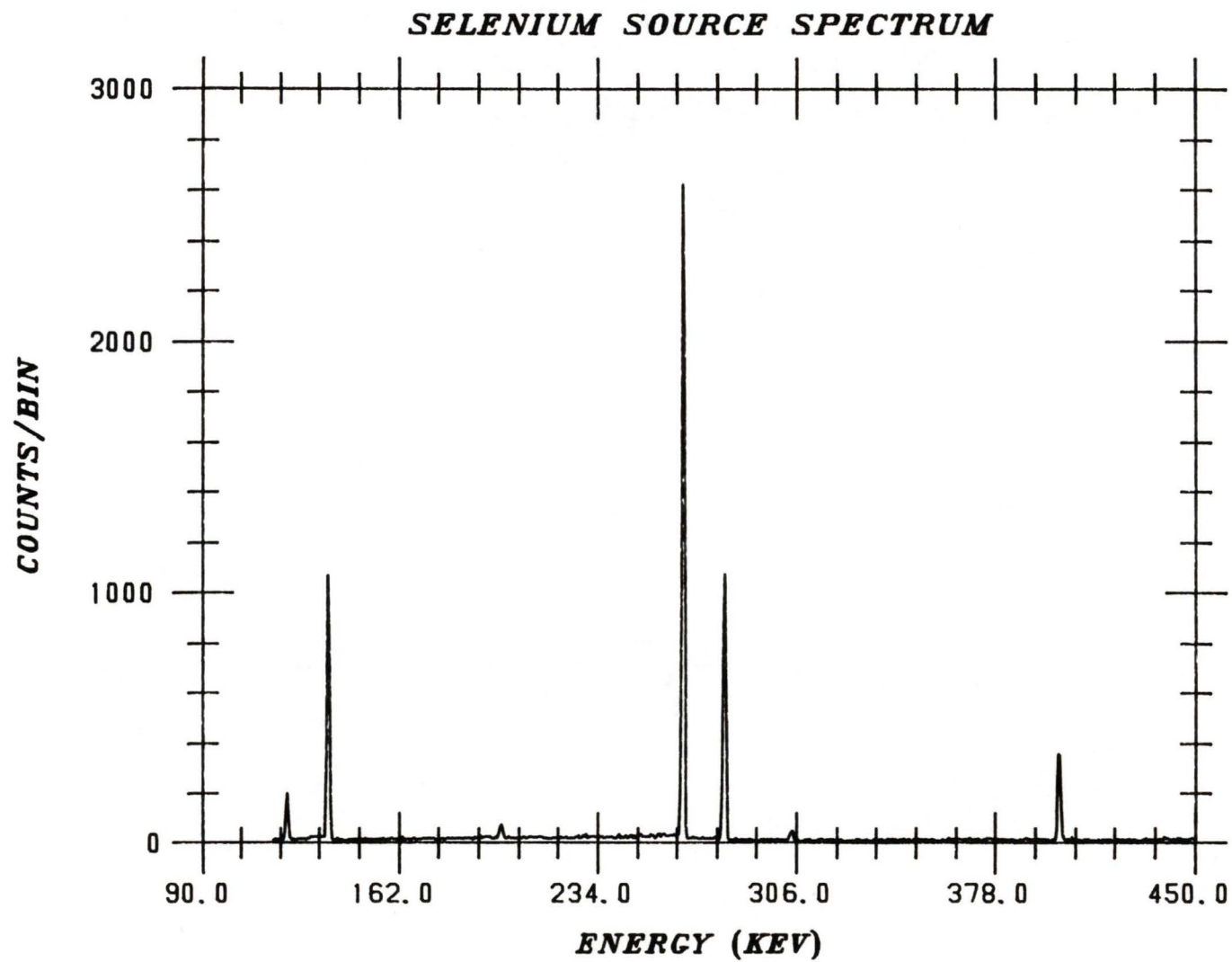


FIGURE 22.

RELATIVE EFFICIENCY OF SELENIUM SOURCE

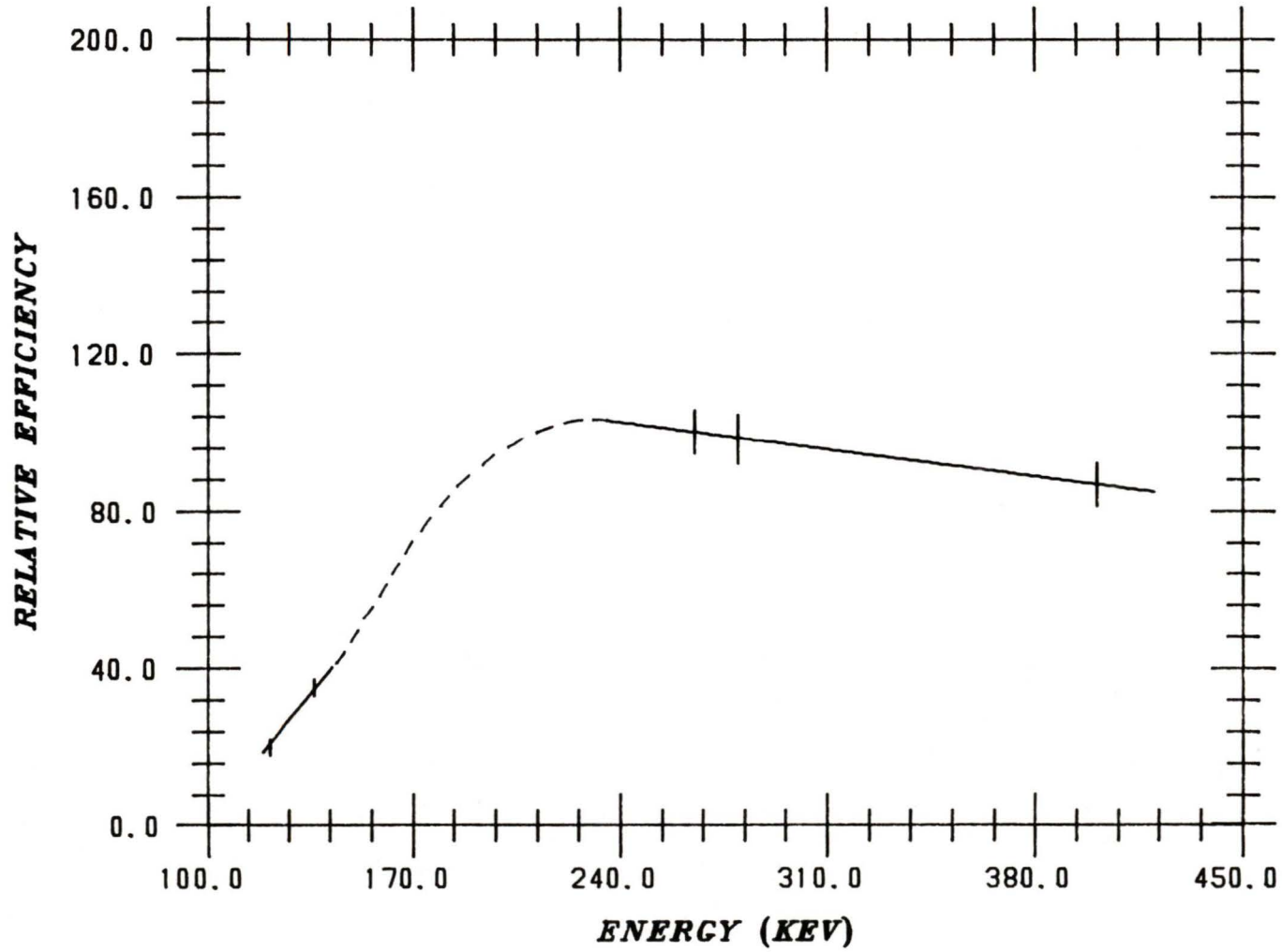


FIGURE 23.

Analysis of the Sodium X-Ray.

Using the values determined for the resolution, tailing and efficiency, fits can be made to the region of the prompt spectrum containing the broad X-ray. One of the most important factors in determining the width of the X-ray is the level and slope of the background. For this reason, three different energy windows were examined, (Figure 24), the normal window being #2 from 234 keV to 306 keV. The small window (#3) represents that used in the analysis of a previous experiment (0L78a), whilst the larger region (#1) required rebinning of the data and thus some loss of information.

The main peaks in the normal window are shown in Figure 25, though the muonic peaks were ignored rather than fitted. In addition to these visible peaks, there is also a Compton edge due to the sodium 440 keV gamma that lies at 278.21 keV. As explained in Chapter 4, the effect of the suppressor is to convert the Compton edge to a broad peak. In order to fit this, a spectrum was acquired using an activated gold source, whose principle peak is at 412 keV. The gold Compton edge (peak) was fitted with a Gaussian-Lorentzian convolution on a linear background, and the result was scaled in energy and intensity to represent the Na 440 γ Compton edge. Finally the Doppler broadening of the 440 keV peak was accommodated by assuming this would broaden the Compton peak in a linear manner. This effect was negligible.

When this Compton edge was included in the fits, the effect was found to be small, and although it was included in the fitting procedure, its entire contribution was considered as part of the

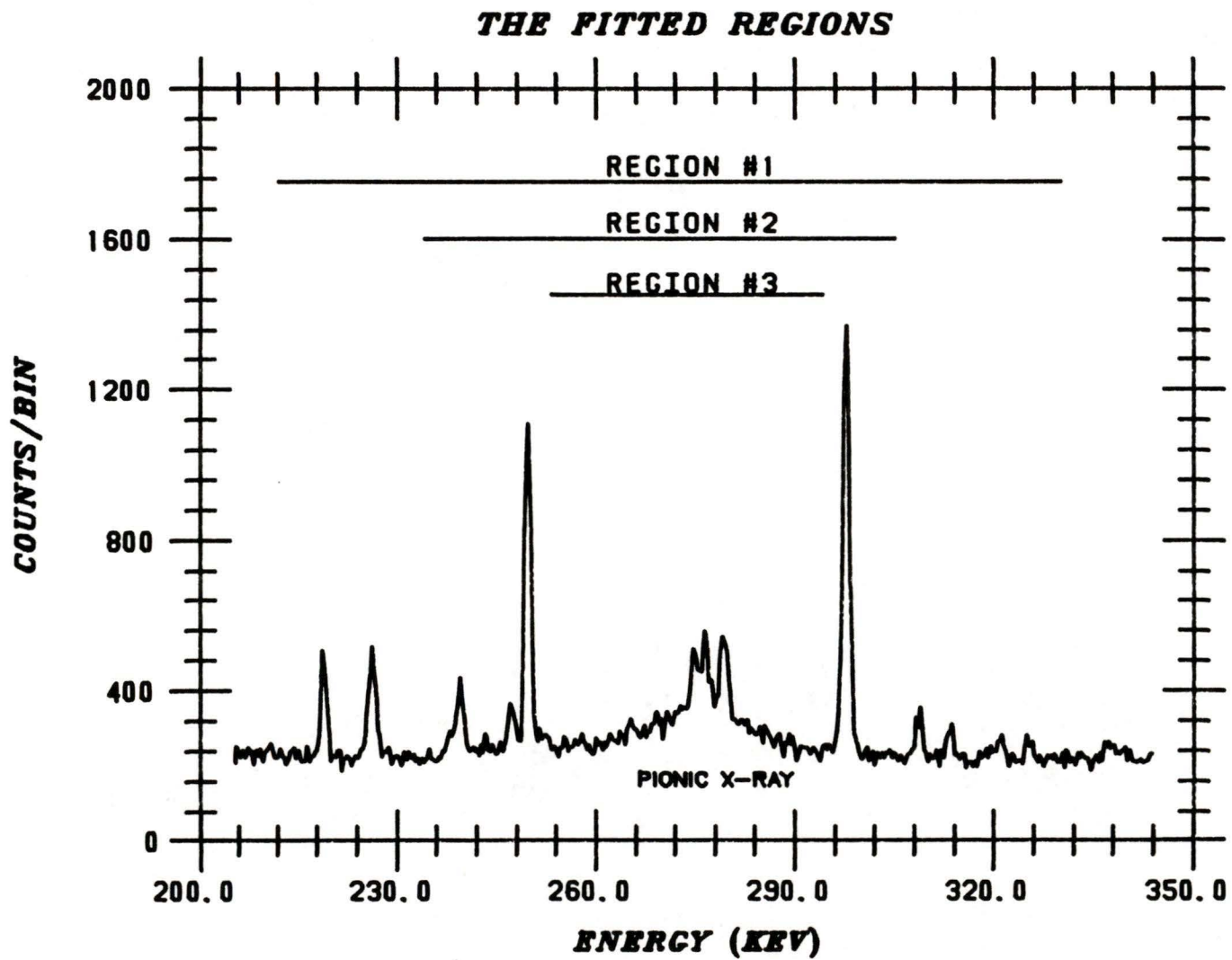


FIGURE 24.

PEAKS IN THE NORMAL FIT REGION

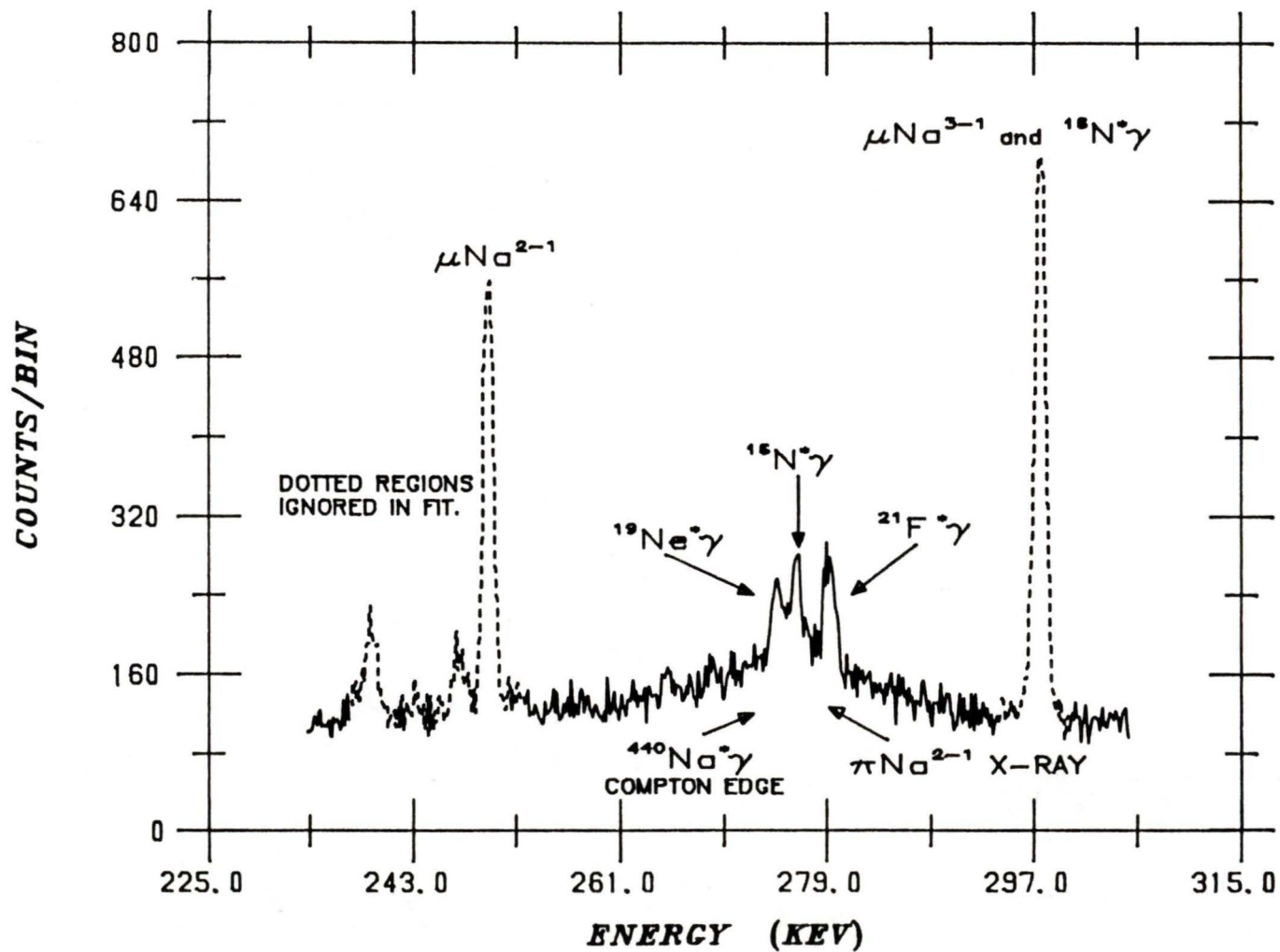


FIGURE 25.

uncertainty in the result. This is a considerable improvement over previous work and arises from the use of a thin NaH target together with the suppression system.

It was found that the choice of fitting window was an important consideration in establishing the background. In particular, with the analysis restricted to the region analysed in the previous run (#3), much the same result was obtained for the X-ray width. This narrow value for the width was due to a higher background than was obtained from the other two windows fitted, and if the shape of this fit was extended to the bigger regions a poor fit was seen. (See Figure 26.) The two wider windows produced results similar to each other. In the final fit the background was fixed in the normal region (#2) from the larger region, (#1). A careful check was made to avoid the Compton edges of higher energy contaminants.

The backgrounds used were linear with energy, but a modification to the fitting program was introduced to test the effect of an exponential background. The effect proved to be negligible in this case.

Close examination of the three contaminant peaks on top of the sodium X-ray suggested the possibility of two further peaks in that area (Figure 27). In particular, the ^{21}F peak, which also appears in the delayed spectrum, had a FWHM 20% wider than expected. So fits were carried out with 5 peaks on top with their position and amplitude being free parameters. The result was a considerable reduction in

EXTRAPOLATED FIT FROM SMALLEST REGION

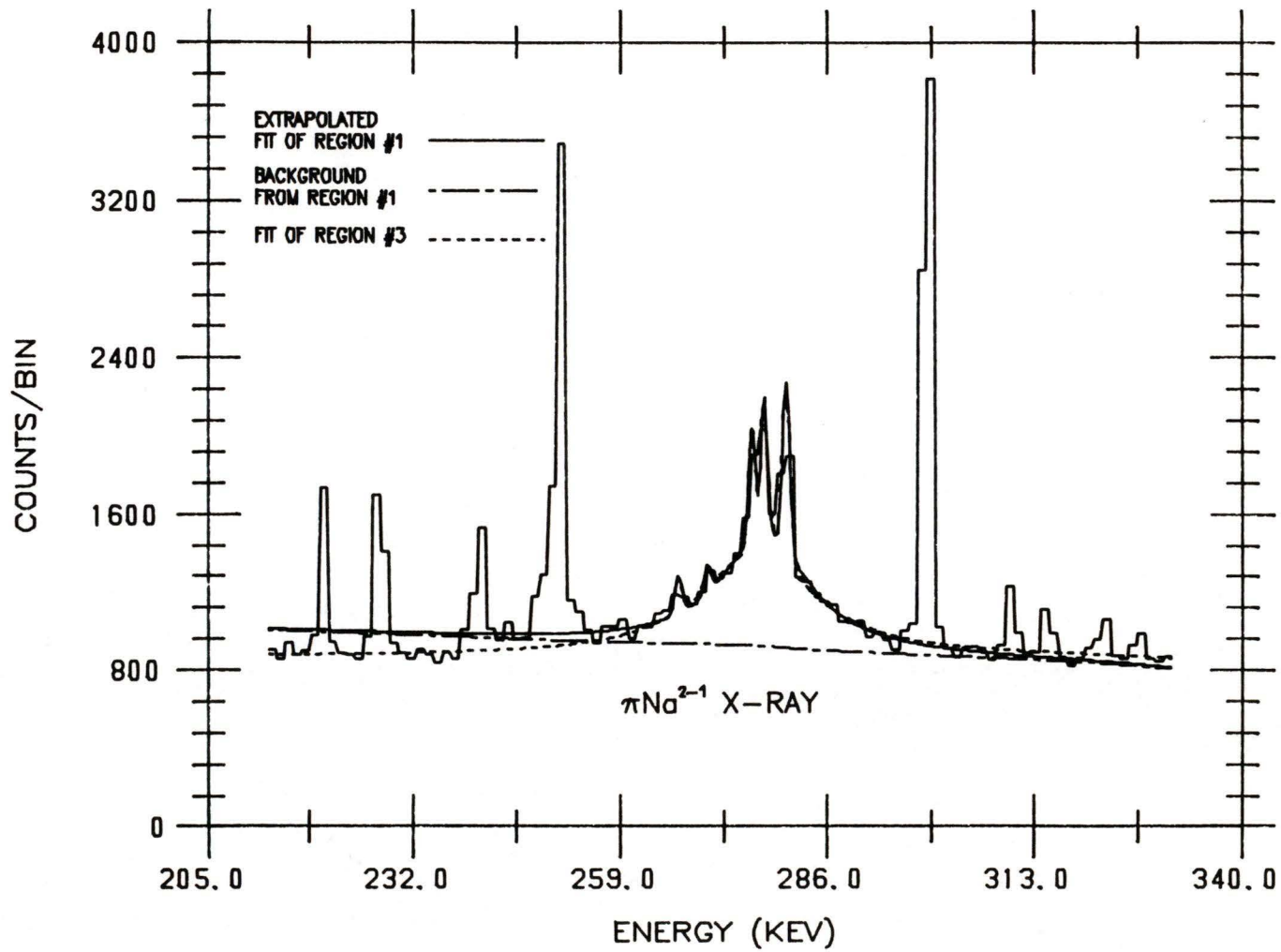


FIGURE 26.

CONTAMINANTS NEAR THE CENTROID OF THE X-RAY

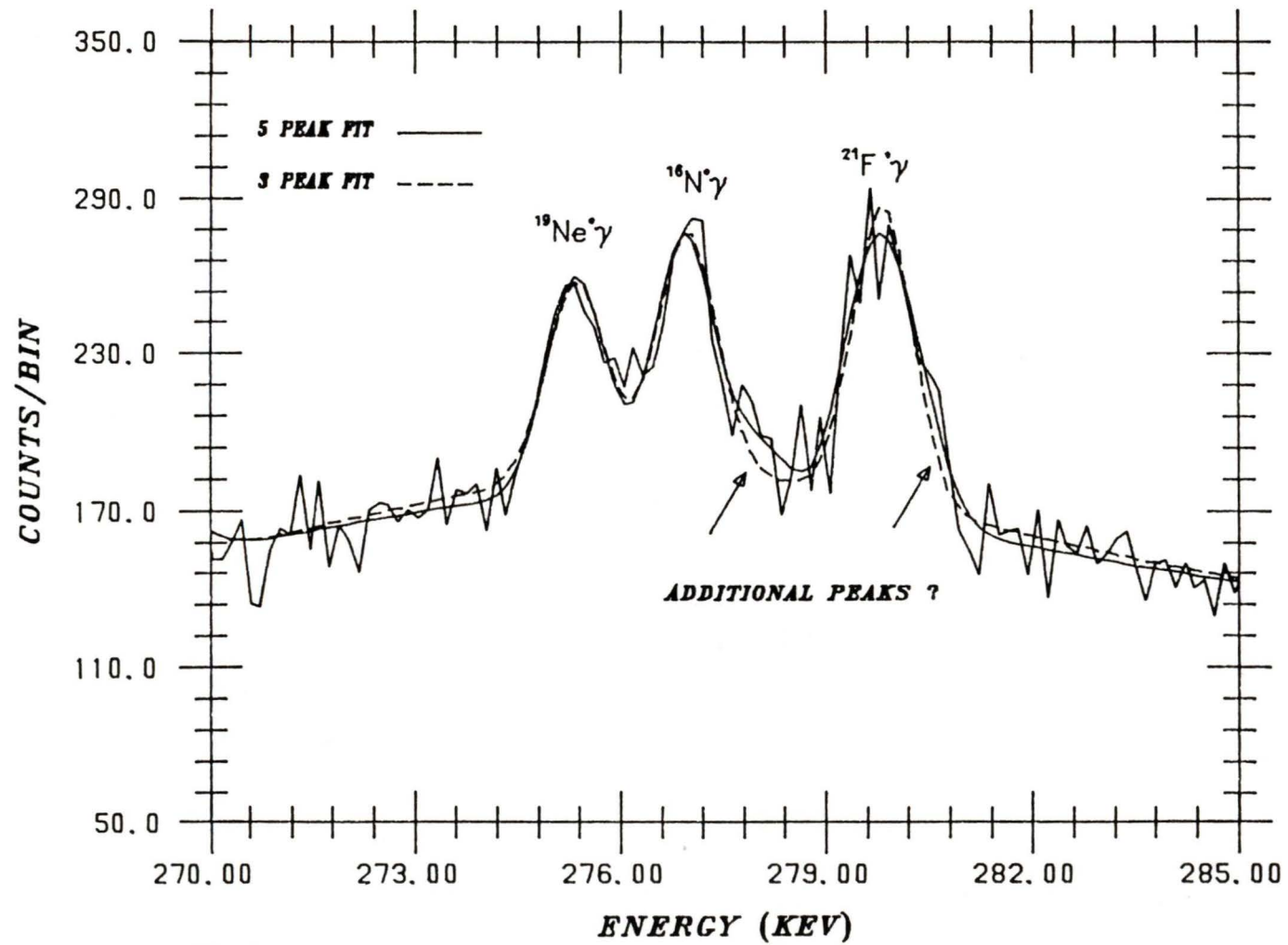


FIGURE 27.

χ^2 per degree of freedom and a startling increase in the width of the X-ray of 2 to 3 keV depending on the background.

No firm identification of these extra peaks was possible. Their intensity was very small and they could easily correspond to two of the many ^{20}F peaks. Some of the more prominent ^{20}F peaks were identified in other parts of the spectrum.

The final fit included these extra peaks, but again their effect was included in the uncertainty estimates.

In view of the effect of small extra peaks overlapping the centroid of the X-ray, the effect of small contaminants to either side of the centroid was also investigated. The standard fits already included two unidentified peaks on the left side, and several more were tried on both sides. The influence of these tended to be more significant on the energy rather than the width of the X-ray. The final fits did not include any of these peaks, other than the standard two, but their effect was considered in the uncertainty.

The final fit was thus composed of the normal region (Figure 28), 5 contaminants on the top and two on the left hand wing, a Compton edge under the X-ray, a linear background fixed from the largest region, and a small tailing correction. The two muonic peaks and a badly contaminated area from 237 to 249 keV were ignored.

The results are given in Table 3, and the contributions to the uncertainty in Table 4.

Table 3. Results.

	Energy (KeV)	Shift (KeV)	Width (KeV)
Pionic Sodium 2-1 X-ray	276.2 (0.9)	-51.0	16.7 (3.1)

Table 4. Contributions to the Uncertainties
in Pionic Sodium.

	Energy (KeV)	Width (KeV)
Statistical	0.27	0.99
Tailing	0.14	0.29
Background and Contaminants	0.41	1.63
Compton edge	0.05	0.02
Efficiency	0.05	0.02
Detector resolution	0.01	0.14
Calibration	Negligible	
Total uncertainty	0.92	3.09

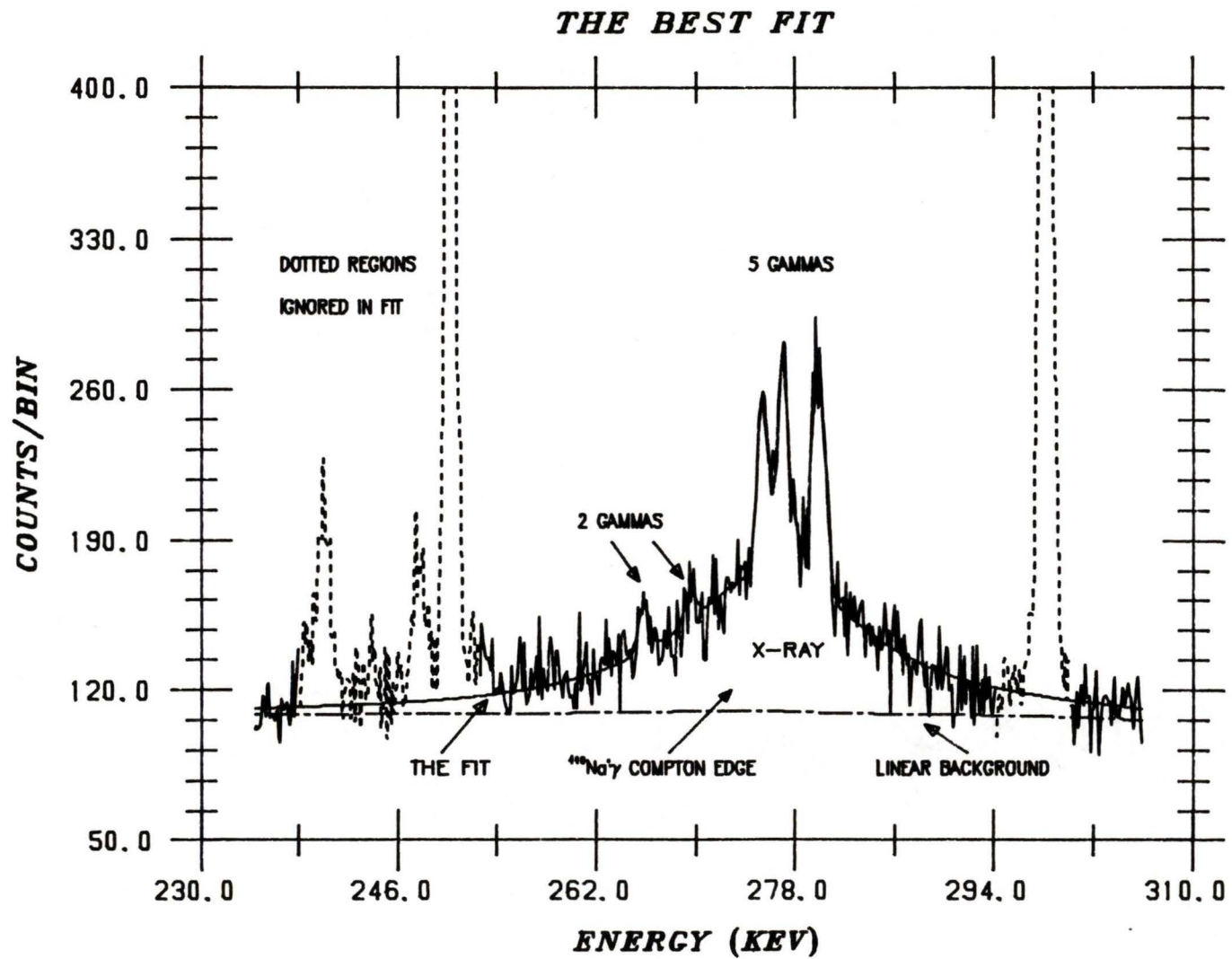


FIGURE 28.

CHAPTER 6: DISCUSSION OF RESULTS AND CONCLUSIONS.

Theoretical Widths and Shifts.

The theoretical width and shift obtained for the sodium pionic 2-1 X-ray, depends on the particular optical potential and parameters used. Poffenberger, in his PhD thesis (P081), performed a global fit of the best pionic X-ray data from light nuclei, and in an attempt to extend this fit to describe sodium, he investigated the large dependence of the sodium width and shift on the neutron distribution. The 'two parameter Fermi' model was used to describe the nuclear density distribution, in the form:

$$\rho(\underline{r}) \propto (1 + e^{(r-c)4\ln 3/t})^{-1} \quad (35)$$

which is characterised by the half density radius, 'c', and the surface thickness, 't'. A selection of Poffenberger's predictions, along with the result calculated by Batty et al. (see Chapter 2), are presented in Table 5. The optical model parameters used by Poffenberger and Batty are shown in Tables 6.

Table 5. Optical Model Fits of Sodium.

Ref.	Energy (KeV)	Width (KeV)	C_n (fm)	t (fm)
Pof.	281.01	24.81	2.25	2.3
Pof.	278.73	20.75	2.52	2.3
Pof.	276.16	17.62	2.92	2.3
Pof.	275.85	17.41	3.00	2.3
Bat.	278.61	21.98	2.69	2.5

Table 6. The Optical Potential Parameters.

Parameter	Poffenberger	Batty
$b_0 (m_\pi^{-1})$	-0.000001	-0.023
$b_1 (m_\pi^{-1})$	-0.102	-0.085
$c_0 (m_\pi^{-3})$	+0.241	+0.21
$c_1 (m_\pi^{-3})$	0.0	+0.089
$Re(b_0) (m_\pi^{-4})$	-0.0501	-0.021
$Im(b_0) (m_\pi^{-4})$	+0.0401	+0.049
$Re(c_0) (m_\pi^{-6})$	--	+0.118
$Im(c_0) (m_\pi^{-6})$	+0.112	+0.058
ξ	1.00	1.00

For a Fermi distribution, the dependence of the R.M.S. radius, 'R', on the half density 'c', and surface thickness 't', is given approximately by:

$$R_n^2 \approx 0.60C_n^2 + 0.71t^2 \quad (36)$$

This allows comparison of the theoretical results from the two fits. Simple calculation shows that the Batty result corresponds to an R.M.S. radius of 2.96 fm, and, accounting for the difference in 't', this would be reproduced by a C_n of 2.89 in Poffenberger's calculations. From Table 5 it can be seen that the corresponding theoretical predictions for the width of the X-ray are about 22 keV by Batty, and about 19 keV by Poffenberger. It should be noted that Batty's global fit was biased towards the 3-2 X-ray transitions, whilst Poffenberger's was based more on the 2-1 data.

A Hartree-Fock calculation performed in 1979 (MA79) has yielded two very different values of R_n , depending on the model used. These values correspond to $C_n = 2.25$ and $C_n = 2.92$. A recent calculation by Wesolowski (WE84), using a semi-empirical formula, has calculated an R.M.S. charge radius of 2.933 fm and since the difference between the neutron and proton distribution is small compared with the above range of C_n , this gives an estimate of R_n . The charge radius from muonic X-rays is 2.986(9) fm (SC78), and from elastic electron scattering 2.940(60) fm. (DE74.)

Experimental Conclusions.

Since the effect of the strong pion-nucleus interaction is to shift the pionic energy levels from the purely electromagnetic values, it is customary to describe pionic X-ray data in terms of a shift, ξ , and a width. The shift is defined as:

$$\xi = E_{em} - E_{expt} . \quad (37)$$

The result of the present analysis of the sodium X-ray is presented in Table 7, along with the other published results, and the theoretical values from the discussion above.

Table 7. Results for the Energy, Widths and Shifts of the Pionic 2-1 X-ray in Sodium.			
Experimental:	Energy (KeV)	Shift (KeV)	Width (KeV)
BA67	276.2(1.0)	-51.0	10.3(4.0)
JE66	277.2(1.0)	-50.0	4.6(3.0)
MI68	277.5(0.5)	-49.7	6.2(1.2)
OL78a	275.75(0.26)	-51.4	12.0(1.2)
Current Work.	276.2(0.9)	-51.0	16.7(3.1)
Theoretical:	Energy (KeV)	Shift (KeV)	Width (KeV)
P081 ($R_n=2.98$)	276.16	-51.04	17.62
BA83 ($R_n=2.96$)	278.61	-48.6	21.98

Comparison of Results.

There are two striking features apparent in Table 7. Firstly, the experimental width obtained from the present work, is significantly different from the previously determined widths, including that obtained by the same group at TRIUMF in 1978 (OL78a). The second feature, is that this new width is, for the first time, in some agreement with the theoretical prediction.

The main difference between the present experiment, and that performed at TRIUMF earlier, was the use of the Compton suppression system. As has been discussed in Chapter 4, the effect of the suppressor was to reduce the background by a factor of about 5 times. This resulted in a peak:background ratio of 1:2 in this work, in contrast to 1:10 in the previous measurement. In addition, the effect of the suppression system was to transform the awkward Compton edge of the Na 440 keV gamma that lies under the X-ray, into a much more manageable broad peak.

It may seem paradoxical that an improved experimental technique has yielded a result with a bigger uncertainty than that assigned previously. However, this is simply a reflection of the fact that better quality data has allowed the evaluation of effects not previously apparent, in particular, the unfortunate structure of contaminants on the top of the X-ray.

The result obtained in this experiment is the first that is within its experimental uncertainty of any reasonable theoretical prediction. It is interesting to note, that if the two extra

contaminants on top of the X-ray proposed in Chapter 5, could be fully resolved, then the experimental width has been estimated as 17.4 (1.9) keV. The reason for this is that in the final fits the two extra contaminants were included, however, the possibility that they were not real, was incorporated in the uncertainty calculations. This resulted in a systematic correction to the X-ray width to centralise it in the uncertainty range.

Conclusion.

The width of the pionic $2p-1s$ X-ray in sodium is at last consistent with the optical potential model of the strong interaction, that has described many other pionic atoms so well. A more accurate determination of the X-ray width would be interesting, however, it is felt that better statistics is not enough, as the contaminants may still remain unresolved. The position of these contaminants, overlapping the centroid of the X-ray, removes vital and irrecoverable information about the underlying lineshape. The best way to support the present results for sodium, will be the careful analysis of the pionic magnesium $2p-1s$ X-ray, observed in a recent experiment at TRIUMF. Any trend towards a narrower width in sodium, would be expected to be evident in magnesium. Preliminary analysis indicates that this is not the case.

REFERENCES

- BA67 BACKENSTOSS, G. et al., Phys. Lett. 25B (1967) 365.
- BA70 BACKENSTOSS, G., Ann. Rev. Nucl. Sci. 20 (1970) 467.
- BA83 BATTY, C.J., E. FRIEDMAN, and A. GAL, Nucl. Phys A402 (1983) 411.
- BE77 BEETZ, R. et al., Nucl. Instr. and Meth. 145 (1977) 353.
- DE74 DEJAGER, C.W. et al., Atomic Data and Nuclear Data Tables 14 (1974) 479.
- ER66 ERICSON, M. and T.E.O. ERICSON, Ann. of Phys. 36 (1966) 323.
- ER70 ERICSON, T.E.O., The Pion-Nucleus Interaction, Proceedings of the Banff Summer School on Intermediate Energy Nuclear Physics p. 102. Eds. G.C. NEILSON, W.C. OLSEN and S. VARMA, University of Alberta.
- ER81 ERICSON, T.E.O., International Symposium on Mesons and Light Nuclei, Liblice, Czechoslovakia, 1-4 July 1981.
- FA72 FALDT, G., Phys. Rev. C5 (1972) 400.
- FE47 FERMI, E. and E. TELLER, Phys. Rev. 72 (1947) 399.
- FR80 FRIEDMAN, E. and A. GAL, Nucl. Phys. A345 (1980) 457.
- GE77 GEHRKE, R.J. et al., Nucl. Instr. and Meth. 147 (1977) 405.
- G074 GOULDING, F.S., and R.H. PEHL, "Semiconductor Radiation Detectors", Nuclear Spectroscopy and Reactions Part A Academic Press (1974) 289.
- HA83 HAGBERG, E. Private Communication.
- JE66 JENKINS, D. et al., Phys. Rev. Lett. 17 (1966) 1.
- KI55 KISSLINGER, L., Phys. Rev. 98 (1955) 761.

- KR69 KRELL, M. and T.E.O. ERICSON, Nucl. Phys. B11 (1969) 521.
- LA47 LATTES, C. et al., Nature 160 (1947) 453.
- MA79 MANKOC-BORSTNIK, N. et al., Nucl. Phys. A325 (1979) 100,
and P081.
- MI68 MILLER, G.H. et al., Phys. Lett. 27B (1968) 663.
- OL78a OLIN, A. et al., Nucl. Phys. A312 (1978) 361.
- OL78b OLIN, A., "Jagspot: A Code For Fitting Complex Gamma Ray
Spectra", University of Victoria TRIUMF Report VPN-78-2
- OL84 OLIN, A., P.R. POFFENBERGER, and D.I. BRITTON, Nucl. Instr.
and Meth. 222 (1984) 463.
- PA67 PARTENSKI, A. and M. ERICSON, Nucl. Phys. B1 (1967) 382.
- P080 POWERS, R.J. et al., Nucl. Phys. A336 (1980) 475.
- POF80 POFFENBERGER, P.R., PHD. Dissertation, University of
Victoria, 1981.
- SC78 SCHALLER, L.A. et al., Nucl. Phys. A300 (1978) 225.
- ST75 STUEWER, R.H., "The Compton Effect" Science History
Publications. (1975) 351.
- TA74 TAUSCHER, L. and W. SCHNEIDER, Z. Phys. 271 (1974) 409.
- WA53 WATSON, K.M., Phys. Rev. 89 (1953) 575.
- WE84 WESOLOWSKI, E., J. PHYS. G:Nucl. Phys. 10 (1984) 321.
- WH47 WHEELER, J.A., Phys. Rev. 71 (1947) 320.
- YU35 YUKAWA, H., Proc. Phys. Math. Soc. of Japan. 17 (1935) 48.

VITA

Surname: BRITTON Given names: DAVID IORWERTH

Place of Birth: Colwyn Bay, N. Wales Date of Birth: February 25, 1960

Educational Institutions Attended, with Dates of Entering and Leaving:

UNIVERSITY OF NOTTINGHAM, NOTTINGHAM, U.K. 1979 to 1982

UNIVERSITY OF VICTORIA, VICTORIA, B.C. 1982 to 1984

Degrees, Diplomas, Etc., Awarded, with Dates and Names of Institutions:

B.Sc. (Honours) 1982 University of Nottingham

Honors and Awards:

University of Victoria Fellowship, 1982/83, 1983/84, 1984/85

Publications:

A. Olin, et al. Segmented Compton Suppression Spectrometer using
Bismuth Germanate, Nucl. Instr. and Meth. 222, 463 (1984).

A. Olin, et al. Pionic 4F-3D X-rays from ^{208}Pb and ^{209}Bi . Submitted
to Nucl. Phys. A. (1984).

D.I. Britton, et al. Pionic 2p-1s X-rays from ^{23}Na and ^{24}Mg . Book of
Abstracts, Vol. 11, p. L8, PANIC Conference, Heidelberg, July 1984.

PARTIAL COPYRIGHT LICENSE

I hereby grant the right to lend my thesis "The Pionic Sodium 2p-1s Transition" to users of the University of Victoria Library, and to make single copies only for such users or in response to a request from the library of any other university, or similar institution, on its behalf, or for one of its users. I further agree that permission for extensive copying of this thesis for scholarly purposes may be granted by me or a member of the University designated by me. It is understood that copying or publication of this thesis for financial gain shall not be allowed without my written permission.

Title of Thesis:

"The Pionic Sodium 2p-1s Transition."

Author:


David I. Britton.

August, 1984